DESIGNING HIGH-THROUGHPUT CANCER BIOMARKER MONITORING PLATFORM USING NANOPARTICLES

by
Jea Ho Park

A dissertation submitted to Johns Hopkins University in conformity with the requirements for the degree of Doctor of Philosophy.

Baltimore, Maryland

March, 2019

Abstract

Developing high throughput cancer biomarker monitoring platform has been a long demand in cancer research. It can enable early diagnosis and help tracking recurrence of disease which will eventually increase patient's survival rate without deteriorating quality of patient's life. This will help doctors selectively treat patients and utilize precision medicine Most cancer biomarker monitoring studies take following two approaches; invasive and non-invasive method. First requires introduction of functionalized nanoparticles with an invasive way such as needle injection. It is designed to perform *in vivo* experiment where nanoparticles circulate in the body and target specific cancer cells of interest. Current obstacles in biomedical imaging for *in vivo* cancer diagnosis is the synthesis of hydrophilic Quantum Dots (QDs) with emission wavelength in the near-IR, a high quantum yield, stability in water, and relatively small sizes. The optimum wavelength for *in vivo* optical imaging, taking into account the absorbance from melanin in the epidermis, hemoglobin in blood, and water in tissue, is in the range of 700-900 nm. In this study, we successfully synthesized NIR-QDs that meets all these requirements for *in vivo* optical imaging. NIR QDs with emission wavelength > 700 nm, 60% QY, and high stability. High quantum yield was maintained for about 100 hours in water. We also studied circulation and retention of QDs *in vivo*. Fluorescent images showed that after 5 minutes of tail vein injection, QDs traveled throughout whole body and even big veins were easily visible. High fluorescence was maintained up to 100 minutes post injection (p.i.). NIR-QDs mostly cleared out by urine and feces and only 10% accumulated in RES system (especially in liver and spleen) after 24 hours p.i.

Non-invasive method is also widely studied because it is more patient

friendly, does not require a large amount of tumor tissue, and enables regular monitoring. Targeting cancer specific biomarkers from a collection of patients' bodily fluids such as urine and blood is actively investigated. For example, about 10 million men take a serum prostate specific antigen (PSA) test for prostate cancer, the second leading cause of cancer death in men in the USA. Due to its high controversy, alternate test methods are developed, including testing genomic biomarkers such as PCA3 and fusion genes. Identifying genetic diversity is important as it can provide insights on disease progression and treatment. In our study, we have tested a panel of prostate cancer genetic biomarkers (AMACR, PCA3, PSMA, TMPRSS2-ERG fusion genes) with oligonucleotide sandwich assay using gold nanoparticles (AuNPs). We established high sensitivity and throughput by controlling oligos conjugated to AuNPs. Using this *in vitro* test, patient urine samples are tested to find correlation between expression of panel of genetic biomarkers and clinical outcomes. We found that patients with same Gleason score and PSA result showed different TMPRSS2-ERG fusion gene expressions. This indicates that oligonucleotide sandwich assay can provide a very important insight on disease progression that conventional tests could not.

Dissertation Committee:

Dr. Peter C. Searson

Dr. Hai-Quan Mao

Dr. Kalina Hristova

Dr. Honggang Cui

Dr. Kwan Hyi Lee

Acknowledgments

First, I want to thank my PI, Dr. Peter Searson for having me as his student. He has been a great mentor and advisor for the last thirteen years and taught me what a great mentor and advisor should be. I am very grateful for the privilege of being his student. I wouldn't be here without his guidance, support, kindness, and patience.

I want to thank Professor Hai-Quan Mao, Kalina Hristova, Hoggang Cui, and Kwan Hyi Lee for their support in serving as my thesis committee. I would also like to thank Dr. Kwan Hyi Lee and Dr. Hyojin Lee for their guidance and support from KIST for the last three years.

I am very thankful for my friends and colleagues, Dr. Minsuk Jung, Bryan Kim, Dr. Jeff Jung, Dr. Chloe Kim, Dr. Janice Lin, Dr. Justin Galloway, Dr. Yu-Ja Huang, Dr. Travis DeJournett, Dr. Hyo-Eun Bhang, Dongjin Lee, Sungwook Park, Dr. Youngdo Jeong, who made my long journey entertaining. I also want to thank all alumni and current members of Searson Group and KIST lab.

Finally, I'd like to thank my parents, Min-Hwa and Yoon-Shin, for their sacrifices, unconditional love and support. I also thank my sister, Evelyn, for always being there and understanding for me. I also thank Hansaem and Nathan (Heeram) for bringing the joy and light to our family. I couldn't have finished this long journey without you.

Table of Contents

List of tables

List of Figures

Chapter 1

Introduction

In cancer research, improving survival rate without deteriorating patient's life quality is considered as a holy grail. To achieve this, high throughput cancer specific biomarker monitoring platform is the key. Usually many studies can be divided into two big approaches; invasive and non-invasive method. This work covers one of the most promising technique for each approach, *in vivo* biomedical using QDs (invasive) and *in vitro* oligonucleotide sandwich assay using AuNPs (non-invasive).

Chapter 1 introduces biomedical imaging using QDs. It is considered as invasive method because QDs are introduced via tail vein injection. Semiconductor QDs have many advantages over conventional dyes; high quantum yield, narrow emission spectra, broad excitation spectra, high threshold for photobleaching, size dependent optical properties that are applicable in fields such as solar cells,[1] light emitting diodes,[2] and biomedical imaging. [3-5]

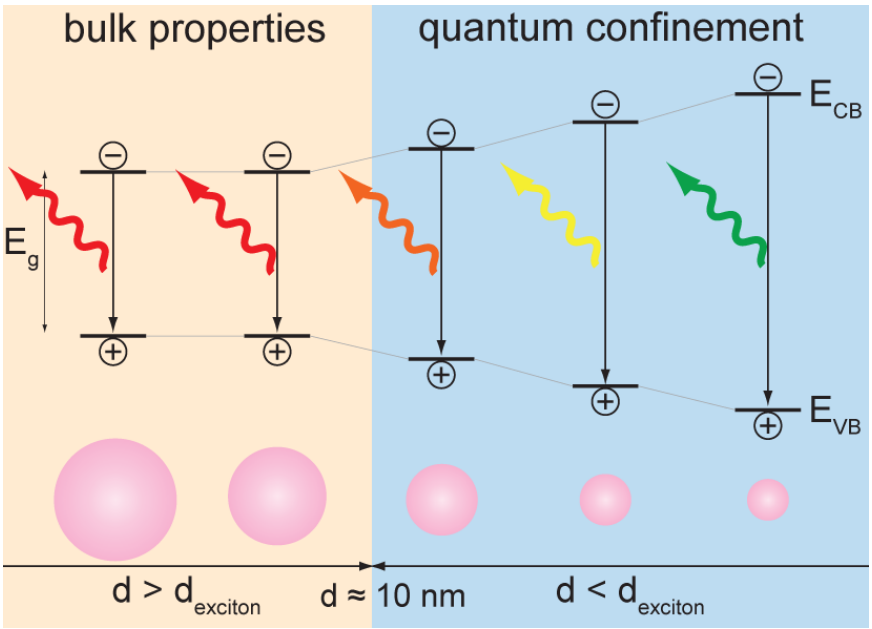

Figure 1.1. Quantum confinement effect of semiconductor nanoparticles. Band gap between valence band and conduction band increases as the size of a nanoparticle decreases below diameter of exciton..

QDs exhibit size dependent properties (**Figure 1.1**). As the particle diameter decreases below about 10 nm, band gap enlargement becomes significant and different emission can be achieved for different particle sizes (**Figure 1.2**), The most common synthesis route for QDs involves an organometallic precursor in a coordinating solvent. Typically precursors are reacted in trioctylphosphine oxide at elevated temperature, usually about 300 °C. The reaction can be performed very simply by injecting the precursor mixture into the solvent with the capping ligand at 270 °C. We also show that growth can be quenched by injection of dodecanethiol. It usually takes one day to synthesize the core and another day to apply coating. Sometimes, multiple coating layers are applied in order to achieve high quantum yield and stability. In this study, we have reduced synthesis time of core/shell NIR QDs to 5-6 hours total from two days using one-pot synthesis.

It is very important to optimize synthesis of QDs with small size, narrow size distribution, high quantum yields, and high stability in water suitable for *in viv*o study. QD synthesis is relatively straightforward, involving mixing the precursors in an air-free environment at elevated temperature. However, subsequent transfer to water and functionalization have many pitfalls. These pitfalls are rarely discussed in the literature and very few groups report results from experiments to verify the properties that are claimed. Thus stability of QDs are demonstrated in this study as well as their circulation *in vivo*.

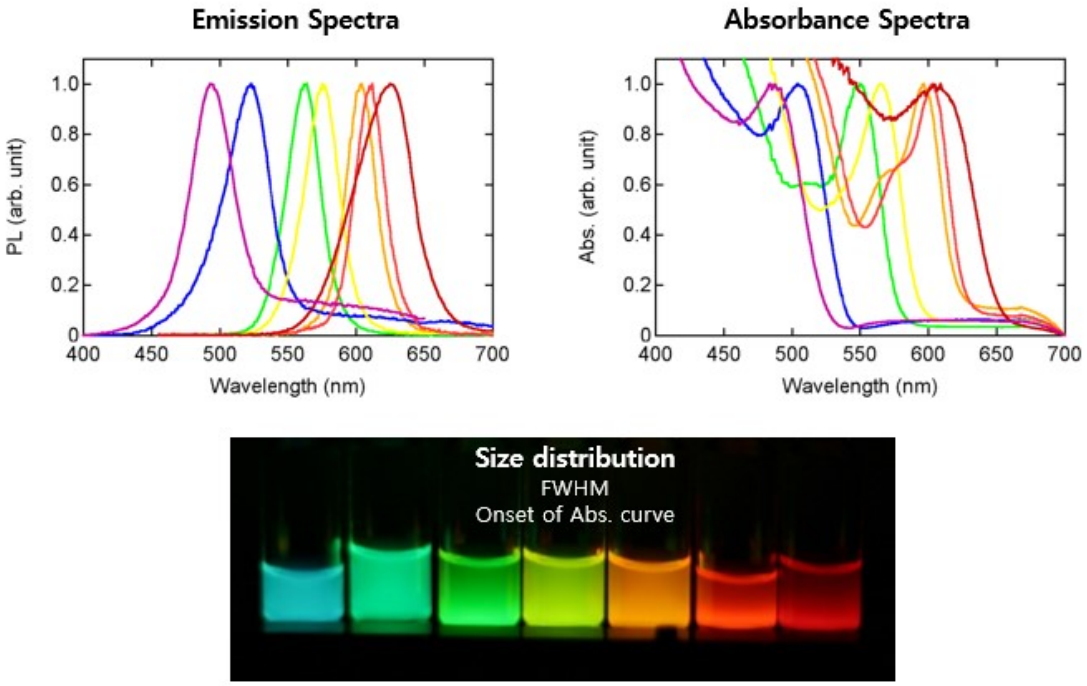

Figure 1.2. Size dependent emission and absorbance spectra of quantum dots. As size of QDs decreases, emission and absorbance spectrum shift to left (towards lower wavelength) and emits different fluorescent colors (blue: smaller, red: bigger).

Chapter 2 introduces a high throughput genomic biomarker monitoring platform using oligonucleotide sandwich assay for prostate cancer. The prostate is a male organ located below the bladder and in front of the rectum. It produces a fluid that makes up semen with sperm cells and fluids from other glands.[6] Most prostate cancers are adenocarcinomas that grow slowly.[7] Prostate cancer is the second most common cancer worldwide[8] and is expected to grow to 1.7 million new cases and 499,000 deaths by 2030.[9] It is the second leading cause of cancer death in men in the US and a recent study predicts 180,890 new cases and 26,120 deaths in 2016.[10] One reason for the high number of new cases is the lack of accurate screening methods resulting in over-diagnosis.[11,12]

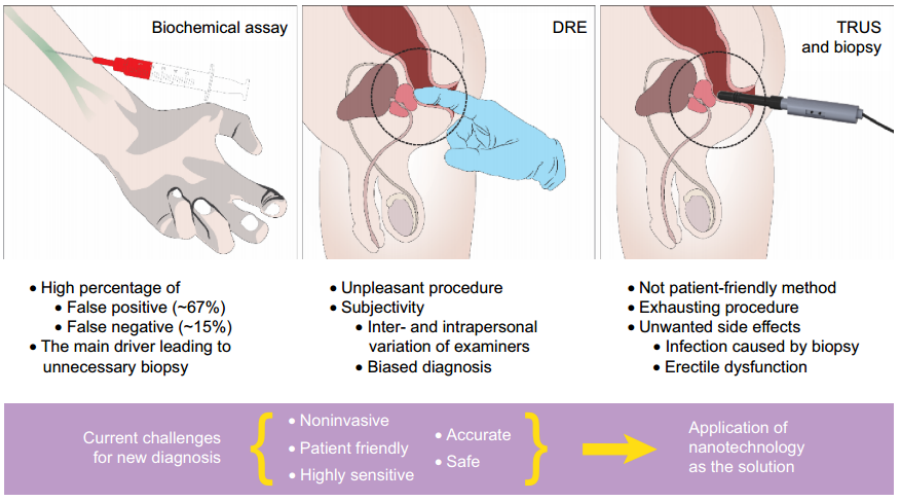

Figure 1.3. Common diagnostic methods for prostate cancer: biochemical assay (PSA test), DRE, and TRUS. The PSA test has a high false positive rate which can lead to unnecessary biopsies. DRE and TRUS have limited diagnostic capability and hence there is a high demand to develop more accurate and safe screening methods.

Screening and diagnosis of prostate cancer usually involves a blood test, rectal exam, and biopsy (**Figure 1.3**)[12]. The two most widely used screening methods are the serum prostate specific antigen (PSA) test and the digital rectal examination (DRE).[12-15] PSA levels above 4 ng/mL are considered to indicate a high chance of prostate cancer and DRE is used for further investigation. A combination of these methods determines whether or not to perform a biopsy.[12,16] After collecting biopsy samples, usually by transrectal ultrasonography (TRUS), a pathologist provides a Gleason score based on the morphology of the growth. Low Gleason scores usually indicate an organ-confined cancer, which is less likely to spread.[12,17,18] Due to the low specificity of the PSA test, clinicians use multiple methods to confirm the presence of disease. Together, the series of tests are time consuming and require multiple hospital visits. In addition, it is very challenging to accurately diagnose a patient with PSA level close to cut-off level and a tumor volume that is difficult to detect via DRE.

Screening for prostate cancer is problematic since the PSA test has a high rate of false positives (66-76%) and false negatives (15%), leading to over-diagnosis (15-66%).[11,19-24] In addition, the DRE alone is not sufficient to provide accurate result.[20,21] Elevated PSA levels may result from many other factors including infection, inflammation, a DRE test, as well as pancreatic cancer.[25-32] Therefore, the U.S. Preventive Services Task Force recommends against PSA screening test due to its potential for side effects and poorly defined benefits,[33,34] and can often lead to unnecessary prostate biopsies. In order to overcome these limitations of PSA test, PHI and 4k score are developed. They are the variation of PSA test in which the level of 3 or 4 serum proteins are measured individually and calculated a score using a mathematical formula.[35-39] Many studies show improvement over PSA test alone, but they cannot provide a reliable diagnosis for prostate cancer. They need to be performed as supplemental test providing information about whether to repeat biopsy or not during active surveillance after a prior negative biopsy result or PSA test.

Of the 180,000 patients diagnosed every year in the US, about 60,000 have low grade prostate cancer where the emerging standard of care is active surveillance or watchful waiting. The motivation for decreasing the number of prostate resections is due to the side effects of the surgery, which include decreased quality of life due to pain, fever, bleeding, infection, and transient urinary difficulties.[34] During watchful waiting, patients receive treatment only if they develop symptoms. The Prostate, Lung, Colorectal and Ovary (PLCO) trial in the US reports 2 death per 10,000 patient from 7 annual screenings with PSA and DRE, whereas, 1.7 deaths per 10,000 was recorded from the control group.[14] Since current screening methods may cause more harm than benefit, the number of patients undergoing watchful waiting is increasing.[13] Therefore, there is a high demand to develop a screening method that can identify patients with

intermediate and high grade prostate cancer, minimize unnecessary biopsies, and provide useful information during watchful waiting.

Gene type	Characteristics	Specificity
AMACR	Prostate cancer enriched	58-80% in serum, 84% with PCA3
PCA3	Prostate cancer specific	76%
PSMA	Prostate cancer enriched; not prostate specific	41%
TMPRSS2-ERG fusion genes	Prostate cancer specific	50% of prostate cancer from PSA screened surgical cohorts

Table 1.1. Urinary genomic biomarkers for prostate cancer

To establish a gold standard test for diagnosis of prostate cancer requires identification of one or more biomarkers.[40-45] Previous studies have shown that a panel of biomarkers can increase sensitivity and specificity.[44,46-50] Studies show 10% increase in sensitivity[44,51] (up to 94% sensitivity with a specificity of 98%) when a panel of genetic biomarkers were used.[51] This suggests that the simultaneous detection of multiple biomarkers can increase the overall reliability (sensitivity and specificity) of prostate cancer screening. Four genetic biomarkers have been chosen for this study based their relation with prostate cancer: α-Methylacyl coenzyme A racemase (AMACR), PCA3, prostate-specific membrane antigen (PSMA), and TMPRSS2-ERG fusion genes.

AMACR on chromosome 5p13 is upregulated nine-fold in prostate cancer tissue compared to normal prostate tissue.[52] AMACR is an enzyme that regulates peroxisomal β–oxidation of branch chain fatty acids.[53] It is present in urine at both protein and

mRNA levels. Previous studies reported 58 - 80% specificity in serum.[54,55] Studies have suggested that expression of this gene in combination with PSA or PCA3, can be used to increase specificity up to 84%, whereas individually it is predictive of prostate cancer.[52,53,56]

PCA3, initially known as DD3, is a noncoding messenger ribonucleic acid (mRNA) from chromosome 9q21-22. PCA3 is overexpressed up to 100-fold in prostate cancer tissue, by more than 95% of all prostate cancer patients.[57-60] Unlike PSA, PCA3 is independent of prostate size, patients' age, and previous biopsies. The PCA3 test has 76% specificity, compared to 47% for the PSA test, and it is only expressed in prostate cancer, not from normal human tissue nor in any other tumor.[44] Even though one PCA3 test (The Progensa) gained FDA approval in 2012,[61] the predictive value of PCA3 alone, and correlation with clinical outcomes, are still in debate.

PSMA is a transmembrane glycoprotein that is upregulated in prostate cancer tissue compared to benign prostate tissues. Expression of PSMA mRNA from urine samples after DRE has been suggested to be more predictive of prostate cancer than PCA3.[62] From the overall group tested in this study, specificity of 41% was observed.[62]

Fusion genes have been regarded as both a diagnostic tool that can be used to monitor patients and therapeutic targets that will be subject to eventual treatment.[63] Gene fusion occurs in various diseases including leukemia, sarcoma, and carcinoma through chromosomal rearrangement.[64] The rearrangement of genes causes a genomic instability in cells, which results in an increased risk for the disease.[63] The prostate cancer overexpresses a specific fusion gene, *TMPRSS2-ERG*, which has a role in tumor progression including invasion and metastasis.[65] *TMPRSS2-ERG* fusions are the most predominant isoform, with multiple studies showing that approximately 50% of

prostate cancers from PSA screened surgical cohorts are *TMPRSS2–ERG* fusion-positive, and greater than 90% of prostate cancers over-expressing ERG harbor *TMPRSS2–ERG* fusions.[48,66]

The current methods employed for detecting these genes are polymerase chain reaction (PCR) and the transcription mediated amplification (TMA) assay.[47,49,67,68] These methods involve RNA extraction, amplification, and normalization.[69-72] Due to the exponential amplification by enzymes, a small amount of genetic contamination or non-specific binding of primers can result in many-fold differences.[71] RNA isolation steps require centrifugation which can result in loss of low molecular weight nucleotides and inconsistent results due to release of nucleic acids from destroyed cells.[73] Measurements from urine samples can be especially challenging and result in low sensitivity,[74] although this can be ameliorated using magnetic beads for capture.[75-77] However, contamination and non-specific binding remain major pitfalls due to exponential amplification.[71]

This oligo-sandwich assay possess many advantages over conventional oligo-based assays.[78] These conventional assays still use PCR after magnetic separation, or chip-based detection which requires chip preparation (surface modification) and silver amplification which results in gray spots that can measure light scattering from each spot. These conventional assays still have similar disadvantages of PCR mentioned above.

To overcome these difficulties, we have developed an oligo sandwich assay, which has high sensitivity and specificity, does not rely on enzymes, and allows multiplexing of a panel of target genes.[79,80] In this study we adapted this assay for quantitative determination of the concentration of a panel of biomarkers for prostate cancer. The assay involves three steps. (1) magnetic microparticles (MPs) modified with an oligo

to capture the target gene, and gold nanoparticles (Au NPs) also modified with a "barcode" oligo to detect the target gene are mixed with the sample. The barcode oligo sequences have a fixed numbers of base pairs to allow quantification by gel electrophoresis. (2) Following magnetic separation, the AuNPs are detached from the MPs and chemically dissolved, allowing isolation of the barcode oligo which has the amplified concentration corresponding to the target gene. (3) Following hybridization the barcode oligo is run in a gel for quantification. We have successfully detected cancer genomic biomarkers for prostate cancer with high sensitivity and also provided a very important insight on disease progression that conventional tests could not.

Chapter 2. Invasive method for *in vivo* biomedical imaging using NIR Quantum Dots

2.1 Introduction

A current challenge in biomedical imaging is the synthesis of water soluble QDs with emission wavelength in the near-IR, high quantum yield, stability in water, and relatively small size. Ideally the synthesis should be relatively straightforward and not involve toxic elements. The optimum wavelength for *in vivo* optical imaging, taking into account the absorbance from melanin in the epidermis, hemoglobin in blood, and water in tissue, is in the range from 700 – 900 nm[81,82] (**Figure 2.1**).

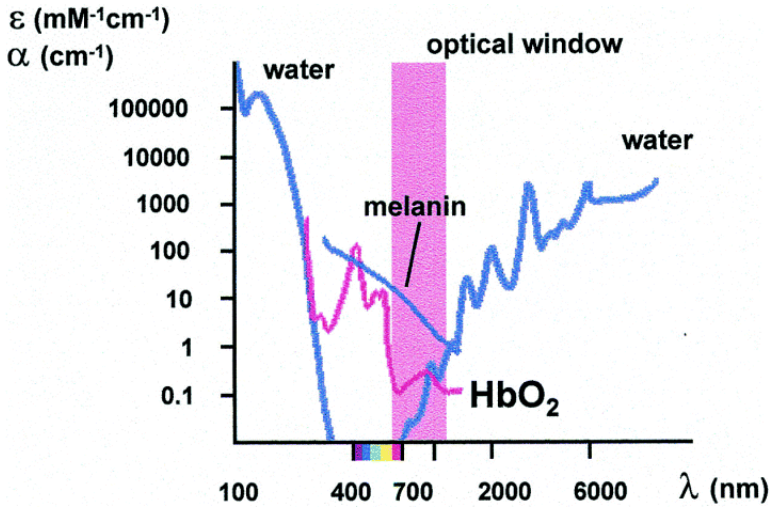

Figure 2.1 Optical window for in vivo study between 7000 – 900 nm where absorptions from melanin, hemoglobin, and water are minimum.

To achieve emission in this optical window, requires a QD with a band gap of around 1.3 - 1.7 eV.[83] Semiconductor QDs that emit in the near-IR, such as CdTe, PbS, InAs, InP, have been synthesized[84-88] and explored for biomedical imaging[89-92]. High quantum yield is important to optimize the signal-to-noise ratio for imaging, and

stability in aqueous solutions is key to avoid aggregation and degradation during imaging. At the same time, it is thought that a hydrodynamic diameter less than about 15 nm is necessary to ensure renal clearance and to avoid accumulation in other organs.[93] In addition, due to concerns over toxicity if QDs are not cleared from the body, it is desirable to avoid elements such as cadmium, lead, and arsenic. Thus there remains a need for the development of QD systems that satisfy all of these requirements. Here we report on the one-pot synthesis of $CuIn_xSe_y$/ZnS core/shell QDs with an emission wavelength $\lambda > 700$ nm. The 20% quantum yield of the core increases to as high as 60% after passivation with ZnS. After thiolation and lipid coating, the $CuIn_xSe_y$/ZnS/DDT/lipid QDs are stable in water for about a week and maintain high quantum yield. We also show fluorescence imaging in a mouse model, illustrating uniform intensity that can be resolved without any image processing.

2.2 Materials and methods

2.2.1. Cu/In Precursor Solution

Copper iodide (0.045 mmol, CuI, Alfa Aesar, puratonic, 99.999%) and indium iodide (0.18 mmol, InI_3, Alfa Aesar, anhydrous, 99.999%) were mixed with trioctylphosphine (3 ml TOP, Strem, 97%) in a glove box. The solution was stirred at 90 ˚C for several hours. The precursor solution was stored in the dark and was stable for up to two weeks.

2.2.2. Core Synthesis

Trioctylphosphine oxide (3.6 g, TOPO, Sigma Aldrich, tech. grade, 90%) and hexadecylamine (6 g, HDA, Sigma Aldrich, tech. grade, 90%) were added to a 100 ml 3-neck flask and heated to 100 ˚C in vacuum to form a transparent solution. The Cu/In precursor solution was injected into the reaction flask and vacuumed for at least two hours. A more concentrated precursor solution can be used (3 times more concentrated) in order to decrease the amount of TOP. Reducing the amount of TOP makes the washing steps somewhat easier. The syringe and the flasks were wrapped with aluminum foil in order to minimize exposure to light. Next, the temperature was increased to 270 ˚C in Ar (Airgas, ultra high purity, grade 5) flow. Bis(trimethylsilyl) selenide (150 µl, $(TMS)_2Se$, Gelest) in TOP (0.5 ml) were mixed in a glove box and injected into the reaction flask. After 6 seconds, 4 ml hexane was injected to quench the reaction. The reaction mixture was then left to cool to 130 ˚C. While injecting hexane into the hot solution, a needle was placed in the septum to avoid a rapid increase in pressure in the flask.

2.2.3. ZnS coating

Bis(trimethylsilyl)sulfide (227 µl, $(TMS)_2S$, Sigma Aldrich, synthesis grade) and diethyl zinc (115 µl, Sigma Aldrich, 52.0 wt.% Zn) were mixed with TOP (1 ml) in a glove box and injected into the suspension of $CuIn_xSe_y$ cores at 130 ˚C. Diethyl zinc is very reactive and should be handled with care. These precursor solutions were placed in a secondary container when transferring from the glove box to the hood to minimize exposure to air. Best results were obtained with fresh chemicals, typically within a month of opening. The amounts of Zn and S were calculated to achieve 3 monolayers (ML) ZnS on the $CuIn_xSe_y$ cores[94]. After injecting the precursors for the shell, the reaction mixture was cooled to 85 ˚C and the QDs annealed for 2 hours. This annealing time was found to give the maximum quantum yield.

2.2.4. OA/TOPO/HDA comparison

The Cu, In, Se, Zn, and S precursors were the same in all experiments. 0.045 mmol CuI and 0.18 mmol InI_3 were mixed in 3 ml of TOP; 150 µl $(TMS)_2Se$; 115 µl diethyl zinc; 227 µl bis(trimethylsilyl)sulfide in TOP.

A. Olyamine (OA). Cores: precursors injected into OA (T = 260 - 290 ˚C; t = 15 - 40 s). Annealing (t = 0 - 1 h) was performed at 100 ˚C. Cores washed with methanol, acetone, ethanol, hexane, or chloroform. Synthesis of ZnS in TOPO/HDA (T = 100 - 240 ˚C). Annealing (t = 0 - 10 h) was performed at temperatures from 100 – 240 ˚C. CIS/ZnS QDs were washed with methanol, acetone, ethanol, hexane, or chloroform.

B. Trioctylphosphine oxide and hexadecylamine (TOPO/HDA). Cores: precursors injected into TOPO/HDA (T = 250 -300 ˚C, t = 2 - 50 s). Annealing (t = 0 to 2 h) was performed at 90 ˚C. Cores were washed with methanol, acetone, ethanol, methanol/isopropyl, hexane, or chloroform. Synthesis of ZnS in TOPO/HDA (T = 130 - 220 ˚C). Annealing (t = 0 - 20 h) was performed at temperatures from 85 - 220 ˚C. CIS/ZnS QDs were washed with methanol, acetone, ethanol, methanol/isopropyl, hexane, or chloroform.

C. One-pot TOPO/HDA. Core precursor injected into TOPO/HDA at 270 ˚C. Reaction time from 6 – 50 s. Synthesis of ZnS in TOPO/HDA (T = 70 - 240 ˚C). Annealing (t = 0 - 20 hours) was performed at temperatures from 85 - 220 ˚C. CIS/ZnS QDs were washed with methanol, acetone, ethanol, methanol/isopropyl, hexane, or chloroform.

2.2.5. Dodecanethiol functionalization

After annealing the $CuIn_xSe_y$/ZnS QDs for 2 hours, dodecanethiol (1 ml, DDT, Sigma Aldrich, ≥98%) was injected into the QD suspension. Final solutions were poured into two 15 ml centrifugal tubes. Methanol and isopropyl alcohol (8:2 by volume) were added to the tubes until they were full. Using stronger solvents degraded the surface of QDs and resulted in aggregation. Too many washing steps (usually more than 3 times) also resulted in aggregation. The QD suspensions were centrifuged at 8000 rpm for 3 minutes. After centrifugation, the precipitate was re-dispersed in hexane and the same washing steps repeated at least twice. The final precipitate was re-dispersed in chloroform.

2.2.6. Water solubilization

DI-water (2 ml) was added to a 5 ml vial. A stirring rod was inserted into the vial to ensure good mixing. This vial was placed in a beaker containing glycerol maintained at a temperature of 110˚C using a hot plate. In a separate vial, polyethylene glycol oleyl ether (0.61 μmol, Brij93®,Sigma Aldrich), 1,2-distearoyl-sn-glycero-3-phosphoethanolamine-N-[methoxy(polyethylene glycol)-2000] (2.43 μmol, DSPE-PEG2k, Avanti Polar Lipids), and 2.3 x 10^{14} QDs were mixed thoroughly. The amount of lipids corresponds to a 20-fold excess of with respect to the amount required for complete coverage of the QDs. This mixture was sonicated and then added drop-wise to the DI-water at 100 ˚C under vigorous stirring for 2 minutes. The solution was then centrifuged at 4000 rpm for 3 minutes and the supernatant filtered through 200 nm syringe filter.

2.2.7. In vivo imaging:

Three mice were prepared for tail vain injection. Special food (TD97184,Teklad Purified Diet, Harlan) was fed a week prior to the experiment in order to eliminate auto-fluorescence from the food. 120 μl QD solution containing 60 μl of QDs and 60 μl of saline was injected into the tail vein and imaged using a Li-cor imaging system in the Small Animal Imaging Facility. The QD concentration was determined from absorbance measurements using an extinction coefficient of 3.1 x 10^6 cm^2 mol^{-1}, based on the number of moles of the solid phase. The extinction coefficient was determined from gravimetric measurements using a density of 3.49 g cm^{-3} for $CuIn_3Se_5$. Fluorescence images were taken at different time points. Procedures were conducted according to protocols approved by Johns Hopkins Animal Care and Use Committee.

2.2.8. ICP-MS

ICP-MS vessels were cleaned in soap, detergent and water mixture, for 16 hours. They were rinsed with DI-water and dried completely. Under the fume hood, vessels were soaked in HCl and HNO_3 for at least 16 hours in each acid. There was no washing required between acids. 27 vessels, then, were prepared for microwave cleaning. 1.5 mL of nitric acid were poured in each vessel. A spacer and membrane were placed then put in microwave. Once they were cooled, 100 uL of samples were mixed with 4.9 mL of HNO_3 and HCl acid. ICP-MS run and data collection were performed by a technician at Johns Hopkins School of Public Health ICP-MS center.

2.2.9. Characterization

Photoluminescence (PL) measurements were obtained using a fluorometer (Fluorolog-3 fluorometer, Horiba Jobin Yvon). Absorbance spectra were obtained using a spectrophotometer (Cary 50 UV/vis). Suspensions of QDs in chloroform or in water were placed in cuvettes with polished sides (Starna Cells, Inc.). Transmission electron microscope images and EDS data were obtained using a Philips EM 420 TEM and FEI Tecnai 12 TWIN. High resolution images were obtained using a Philips CM 300 FEG TEM. Samples for transmission electron microscopy were prepared by placing a drop of the QD suspension on a gold lacey-carbon grid. The absolute QY was measured using an Absolute PL Quantum Yield Measurement System (Hamamatsu, C9920-02). Particle size distributions were measured using a Malvern Zetasizer. A Pearl Impulse Li-Cor system was used for small animal imaging. Pearl Impulse software and ImageJ were used for analysis of fluorescence

images. XRD measurements were performed using a Phillip's X Pert 3040 with a Cu K_α source.

2.3 Results and discussion

2.3.1 One-pot synthesis of $CuIn_xSe_y$ QDs

The $CuIn_xSe_y$ QDs were synthesized by reaction of CuI, InI_3, and bis(trimethylsilyl) selenide ($(TMS)_2Se$) in trioctylphosphine oxide (TOPO) and hexadecylamine (HDA). The Cu:In:Se precursor ratio was 1:4:14. After injection of the precursors at 270 ˚C for 6 s, the reaction was quenched by injection of hexane. Large $CuInSe_2$ nanoparticles have been synthesized from Cu, In, and Se precursors in oleyamine (OA),[95,96] and $CuIn_xSe_y$ QDs have been synthesized from TOPO and OA.[97,98] However, we were not able to grow an effective passivation layer on $CuIn_xSe_y$ cores synthesized in these solvents. After investigating various combinations of the solvents TOPO, TOP, HDA, and OA, we found that the synthesis of $CuIn_xSe_y$ cores in TOPO and HDA with a mole ratio of 1:3 was optimum for one-pot passivation, high quantum yield, and stability in water (**Table 2.1**). The one-pot synthesis produces excellent quantum yield and stability, and also reduces the number of washing steps, synthesis time, and cost, compared to the two-step synthesis. The addition of DDT (up to 1 ml) did not enhance quantum yield, but it significantly improved stability.

Surfactants (number of experiments)	**Core synthesis with QY > 15%**	**Core/shell synthesis with QY > 30%**	**Comments**
OA (36)	19%	0%	QY decreased after ZnS passivation (average decrease 3%, max. decrease 13%)
TOPO/HDA (23)	52%	60%	QY = 32 ± 14 (maximum 50%)
one pot with TOPO/HDA (42)	N/A	60%	QY = 32 ± 11 (maximum 60%)

Table 2.1 Summary of 101 synthesis experiments for CIS and CIS/ZnS QDs.

2.3.2 Optical properties of $CuIn_xSe_y$ QD

Figure 2.2a shows the emission spectrum for $CuIn_xSe_y$ QD cores in chloroform. The emission peak is at 745 nm, well into the optical window for biomedical imaging. The full width at half maximum (FWHM) is about 133 nm. This synthesis is highly reproducible: the emission peak was 759 ± 20 nm and the FWHM was 133 ± 6 nm for 4 syntheses. The quantum yield of the cores was typically 20 – 30%. The absorbance spectrum for the $CuIn_xSe_y$ cores shows an absorption onset at about 800 nm, corresponding to the PL peak. Similar absorbance spectra have reported for $CuIn_xSe_y$ cores synthesized from other solvent combinations.[97-99]

2.3.3 TEM and EDS analysis on $CuIn_xSe_y$ core

Figure 2.2b and **Figure 2.3** show a representative Energy Dispersive X-ray (EDS) spectrum for a $CuIn_xSe_y$ core along with a high resolution TEM images. The EDS spectrum confirms the presence of $CuIn_xSe_y$ with x = 3.3 and y = 4.4, close to the composition of the compound $CuIn_3Se_5$.[100] Detailed analysis of the particle size distribution was difficult due to the poor contrast, however, from analysis of TEM images we estimate an average size of 4.0 ± 0.1 nm (n = 39). The relatively broad FWHM is ascribed to compositional variation since the reported bands gaps of $CuInSe_2$, $CuIn_3Se_5$, $CuIn_5Se_8$, are 1.04 eV, 1.26 eV, and 1.34 eV, respectively.

2.3.4 ZnS passivation

For most applications of QDs, the addition of a wide band gap shell is required to passivate surface states and increase the quantum yield. As we show below, the $CuIn_xSe_y$ cores have limited stability and hence the shell also serves to isolate the core from the environment. The emission peak at about 745 nm (**Figure 2.2a**) implies a

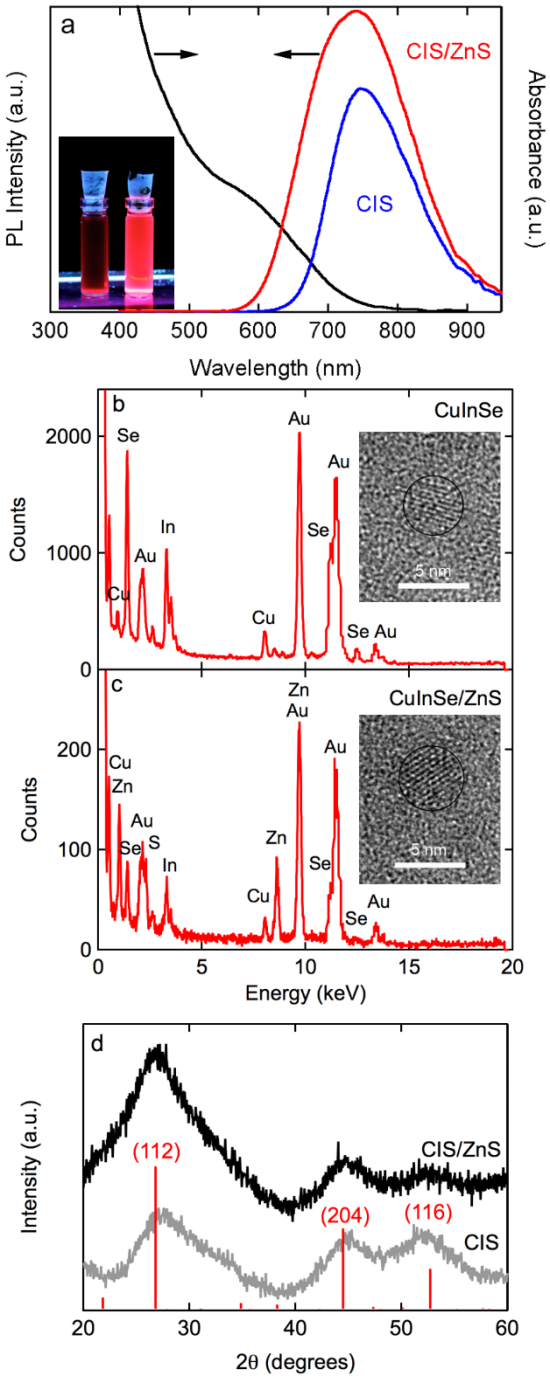

Figure 2.2 (a) Photoluminescence spectra for $CuIn_xSe_y$ (745 nm peak and 133 nm FWHM) and $CuIn_xSe_y$ /ZnS QDs (737 nm peak with 175 nm FWHM), and absorbance spectrum for $CuIn_xSe_y$/ZnS QDs. Inset shows a photograph of suspensions of $CuIn_xSe_y$ (left) and $CuIn_xSe_y$/ZnS (right) QDs in chloroform under UV excitation. The quantum yield increased from 20% to 50% after ZnS passivation. (b) EDS spectrum QDs and high resolution TEM image for a CuInSe QD. (c) EDS

spectrum and high resolution TEM image for a $CuIn_xSe_y$/ZnS QD. The gold peaks in the spectra are from the TEM grid. The average diameter, obtained from analysis of TEM images, is 4.0 ± 0.13 nm for the $CuIn_xSe_y$ cores and 5.0 ± 0.17 nm for the $CuIn_xSe_y$/ZnS core/shell QDs. (d) X-ray diffraction patterns for $CuIn_xSe_y$ and $CuIn_xSe_y$/ZnS QDs. The peak positions for stannite form of $CuIn_3Se_5$ and their relative intensities are also shown

band gap of about 1.66 eV. This is significantly larger than the band gap of 1.26 eV for $CuIn_3Se_5$ and implies significant confinement.[101] We selected ZnS as a passivation layer since it has a bulk band gap of about 3.68 eV, and is commonly used to passivate II-VI QDs.

In addition, the selection of ZnS allows us to avoid possible toxicity concerns by avoiding elements such as cadmium and arsenic. ZnS passivation of $CuIn_xSe_y$ QDs has been achieved after washing and resuspending the $CuIn_xSe_y$ cores in ODE/OA prior to introducing the shell precursors and other reagents.[98] Here we demonstrate successful passivation after injecting $(TMS)_2S$ and diethyl zinc directly into the suspension of $CuIn_xSe_y$ cores.

After the growth of the shell, the emission peak is slightly blue-shifted to 737 nm indicating a small decrease in the size of the core due to the formation of an alloy at the core-shell interface (**Figure 2.2a**). The FWHM is increased to 175 nm indicating broader size distribution resulting from the passivation process.[102-104] The core/shell synthesis produced an average emission peak of 741 ± 12 nm with a FWHM of 175 ± 9 nm for 4 syntheses. The quantum yield for the $CuIn_xSe_y$/ZnS QDs typically increased to 40 – 60%, confirming the importance of the passivation of surface states.

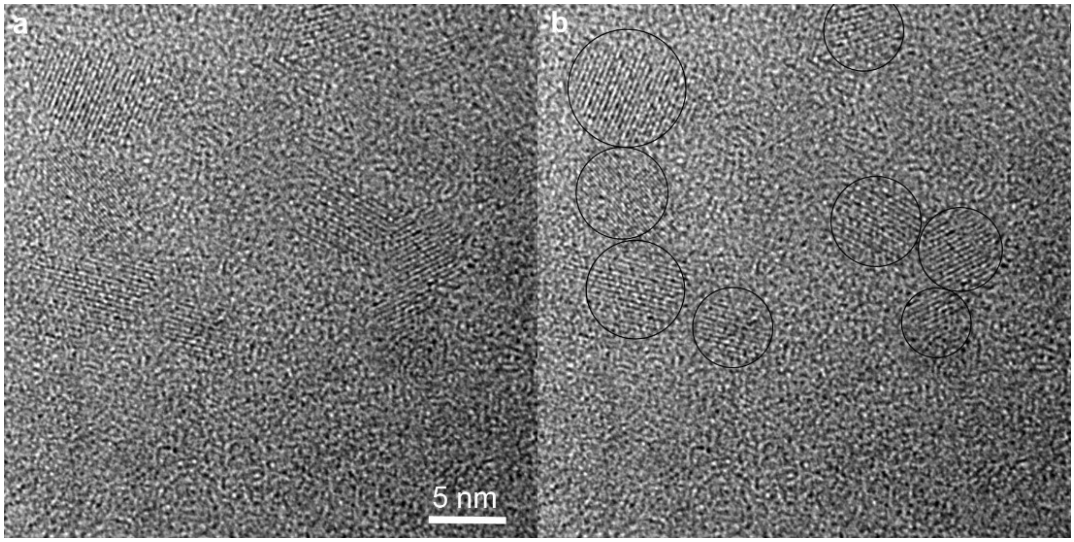

Figure 2.3 (a) High resolution TEM image of several CuInSe QDs. (b) Same image with QDs indicated by circles.

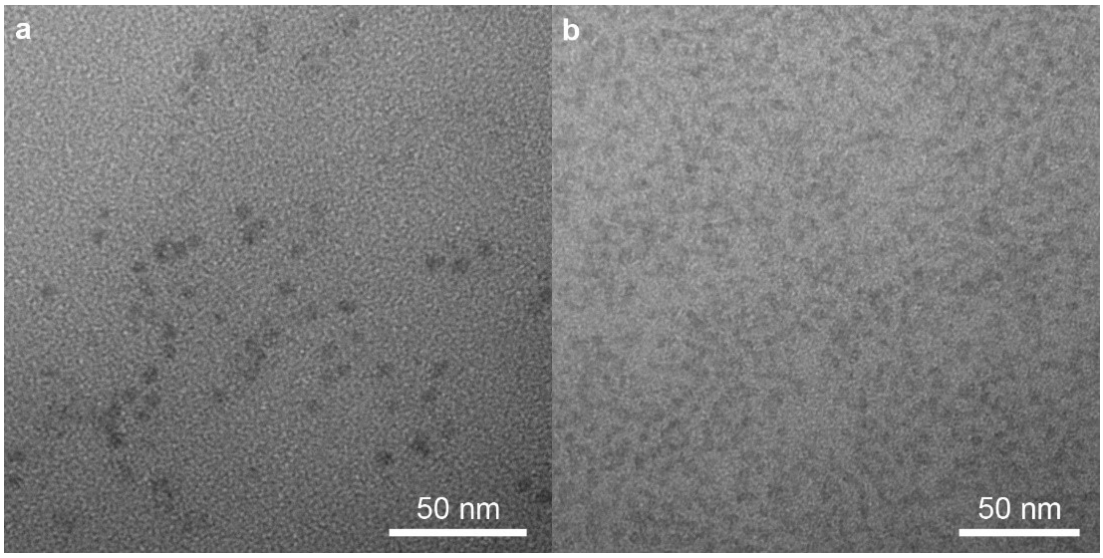

Figure 2.4 Low magnification TEM images of CuInSe/ZnS core/shell QDs.

2.3.5 TEM, EDS, and XRD analysis on $CuIn_xSe_y$/ZnS core/shell QDs

Figure 2.2c and **Figure 2.4** show a representative EDS spectrum for a $CuIn_xSe_y$/ZnS QDs along with a high resolution TEM images. The EDS spectrum (**Figure 2.2c**) confirms the presence of Zn and S in the $CuIn_xSe_y$/ZnS QDs. The average diameter of the core/shell QDs was 5.0 ± 0.2 nm (n = 72). The difference in

average diameter between the cores and the core/shell QDs implies an average QD shell thickness of about 0.5 nm, in agreement with the expected value based on the concentration of precursors. XRD powder diffraction spectra (**Figure 2.2d**) for the cores and core/shell QDs are consistent with the stannite crystal structure (space group $I\bar{4}2m$) for $CuIn_3Se_5$.[100] (**Figure 2.5**)

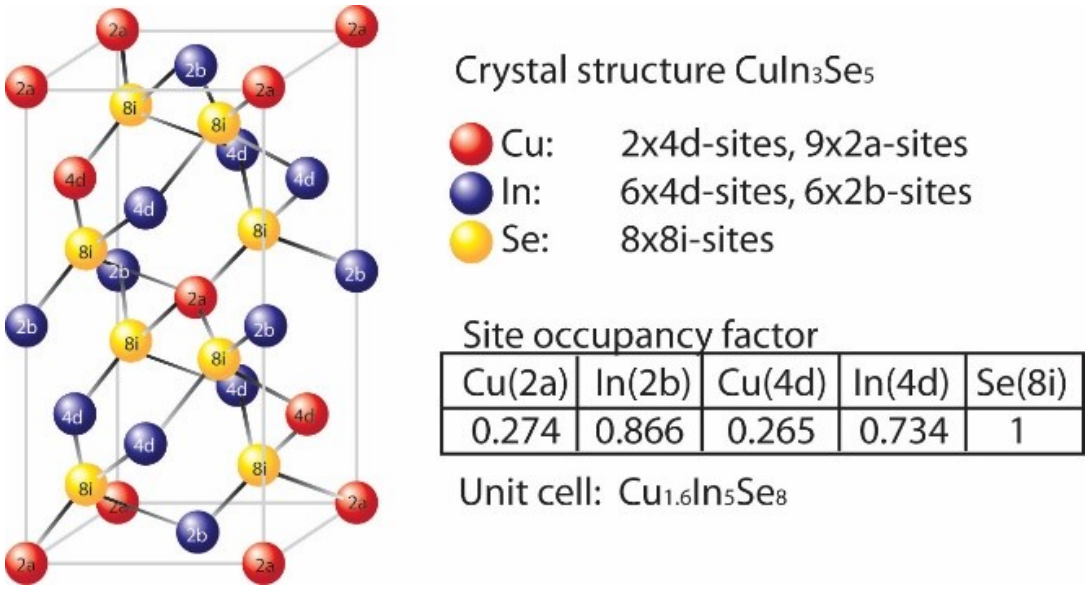

Figure 2.5 Crystal structure of $CuIn_xSe_y$ obtained from EDS spectrum and XRD data. It is the stannite structure with $CuIn_3Se_5$ composition.

2.3.6 Stability of the QDs

The stability of the QDs was characterized by measuring the time dependence of the quantum yield and PL. The quantum yield of the $CuIn_xSe_y$ cores in chloroform decreased rapidly after 1 – 2 days, indicating poor stability. Similar results were obtained for cores synthesized using the method reported by Allen et al.[97] The loss of stability was largely due to aggregation, as inferred from the fact that the emission peak remained constant at about 760 nm and the FWHM at about 130 nm.

The addition of the ZnS passivation layer resulted in an improvement in stability. The quantum yield in chloroform remained in the range 40 – 60% for 1 – 2 days but decreased to 10% after 4 – 5 days. The PL peak remained constant at about 730 nm and the FWHM remained at about 170 nm. Significant improvements in stability were obtained by replacing the TOPO/HDA coordinating ligands by dodecanethiol (DDT). The quantum yield for DDT-modified $CuIn_xSe_y$/ZnS/DDT QDs in chloroform remained high for 10 - 14 days, and decreased to 10% after 21 days (**Figure 2.6a**).

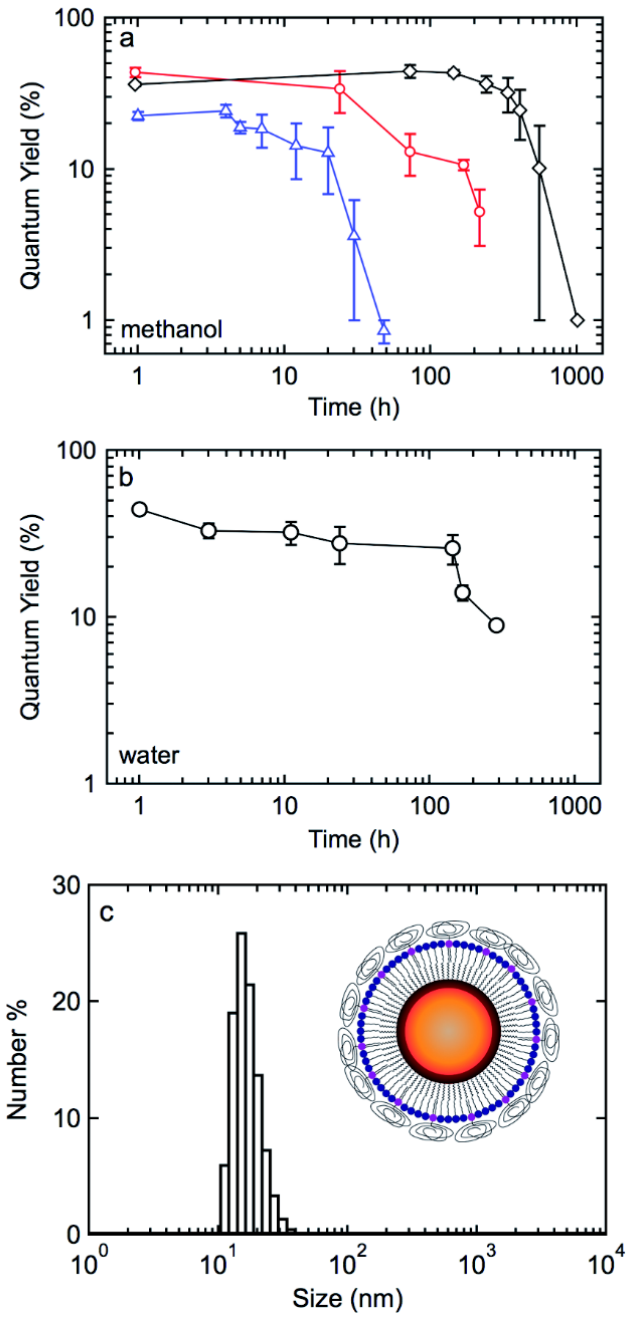

Figure 2.6 (a) Quantum yield versus time for $CuIn_xSe_y$, $CuIn_xSe_y$/ZnS, and $CuIn_xSe_y$/ZnS/DDT QDs in chloroform. (b) Quantum yield versus time for $CuIn_xSe_y$/ZnS/DDT/lipid QDs in water. (c) Size distribution of $CuIn_xSe_y$/ZnS/DDT/lipid QDs in water measured by DLS. The average diameter is 15 nm. The inset shows a schematic illustration of the functionalized QDs.

2.3.7 Water solubilization of QDs

Lipid coating was used to transfer the $CuIn_xSe_y/ZnS$ QDs to water.[105] Various combinations of single acyl chain lipid and double acyl chain lipids with PEG groups were tested. A lipid composition of 80% PEGylated lipid with 20% single acyl chain lipid gave the best results. These lipid coated QDs showed a quantum yield of about 50% QY in water and were stable for at least several days at room temperature (**Figure 2.5b**). After lipid coating, the average hydrodynamic diameter, measured by DLS, was 15 nm (**Figure 2.6c** and **Figure 2.7**). As described above, the core/shell QDs are about 5 nm in diameter. Taking the DDT inner leaflet as 1 nm, the lipid outer leaflet as 2 nm, and the PEG radius of gyration as 2 nm, we expect the overall size to be about 15 nm, in excellent agreement with the measured particle size.

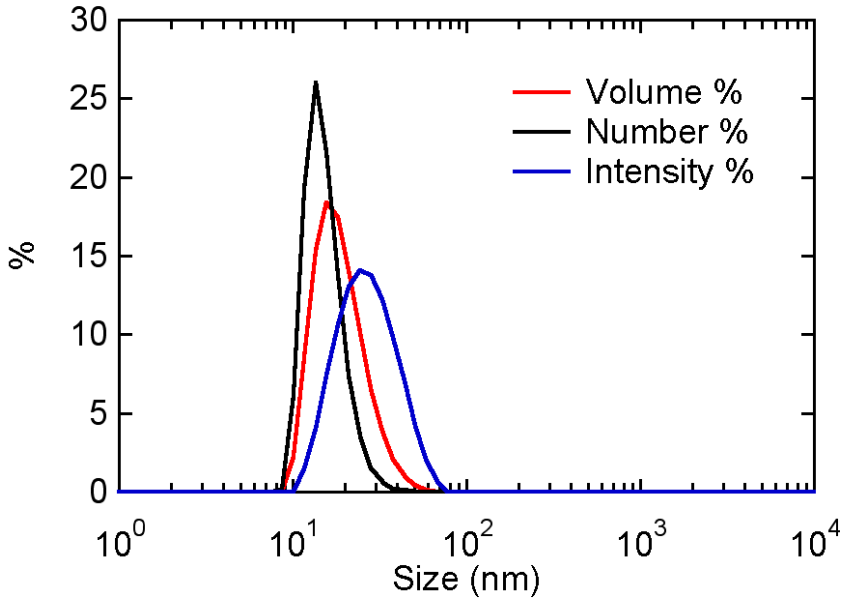

Figure 2.7 Size distribution for lipid coated $CuIn_xSe_y/ZnS$ QDs. From analysis of TEM images, the QDs are 5 nm in diameter. Taking the DDT inner leaflet as 1 nm, the

lipid outer leaflet as 2 nm, and the PEG radius of gyration as 2 nm, we expect the lipid-coated QDs to have a diameter of 15 nm, in excellent agreement with the average obtained from the number density. The relatively small differences between the volume, number, and intensity distributions indicate very small amount of aggregation.

2.3.8 Performance of the $CuIn_xSe_y$/ZnS QDs for biomedical imaging

To explore the performance of the $CuIn_xSe_y$/ZnS QDs for biomedical imaging, we performed fluorescence imaging in mice after tail vein injection. 230 pmol of lipid coated QDs in 120 ul of saline were introduced by tail-vain injection. Fluorescence images were taken as a function of time post-injection (p.i.). **Figure 2.7** shows

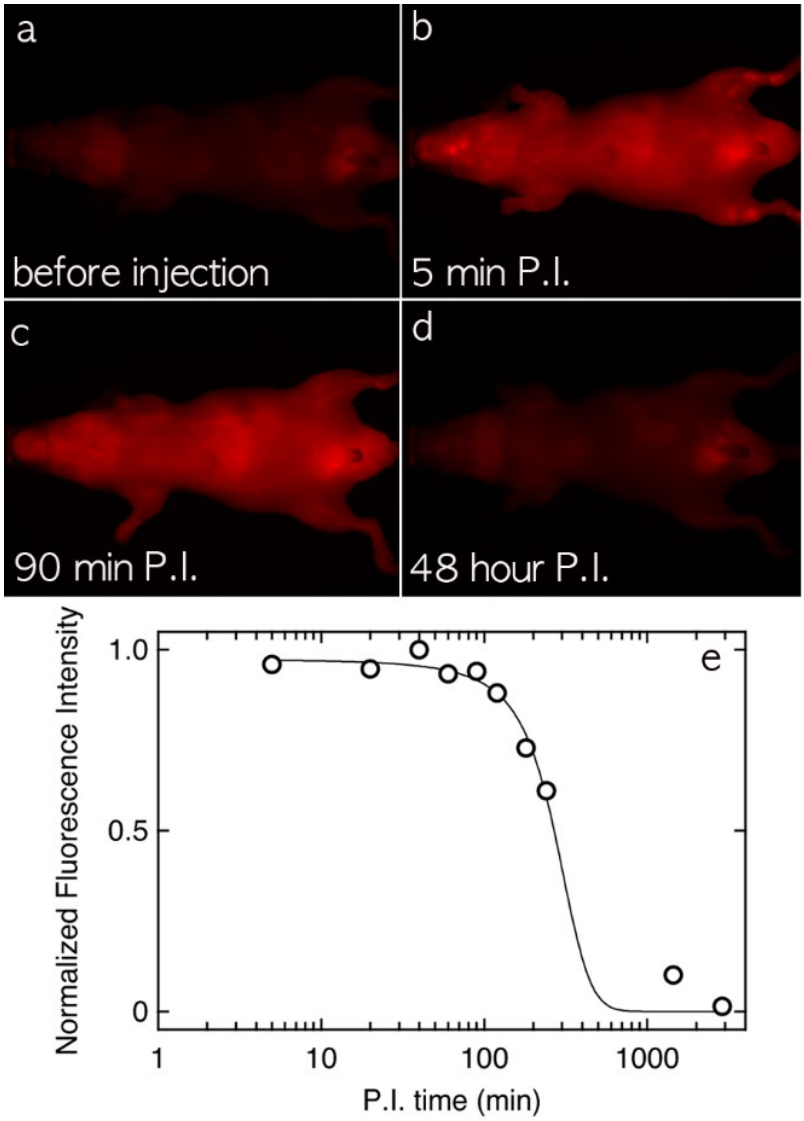

Figure 2.8 Fluorescence images obtained from the ventral side of a mouse after tail vein injection of 230 pmol QDs. (a) Before tail vein injection, (b) 5 minutes post-injection, (c) 90 minutes post-injection, and (d) 48 hours post-injection. (e) Normalized average intensity per pixel (obtained from the fluorescence images) versus time after injection.

fluorescence images recorded before injection, and at 5 minutes, 90 minutes, and 48 h p.i. Immediately after injection (**Figure 2.8b**) the fluorescence intensity increased relatively uniformly over the whole body of the mouse. Indeed, some of the larger blood vessels were easily detectable. The fluorescence intensity started to decay at 90

minutes p.i. (**Figure 2.8c**), and after 48 h had returned to the same level as before injection (**Figure 2.8d**). Very similar results were obtained for the other mice. There are no bright spots indicating aggregation or measurable accumulation in organs such as the liver or spleen, suggesting good clearance from the body although this remains to be confirmed by quantitative analysis. Fluorescence images of the resected organs (**Figure 2.9**) show a similar dependence on time as the dorsal and ventral images; the fluorescence increases to a maximum at about 30 minutes p.i., but then decreases to values close to background after 24 h.

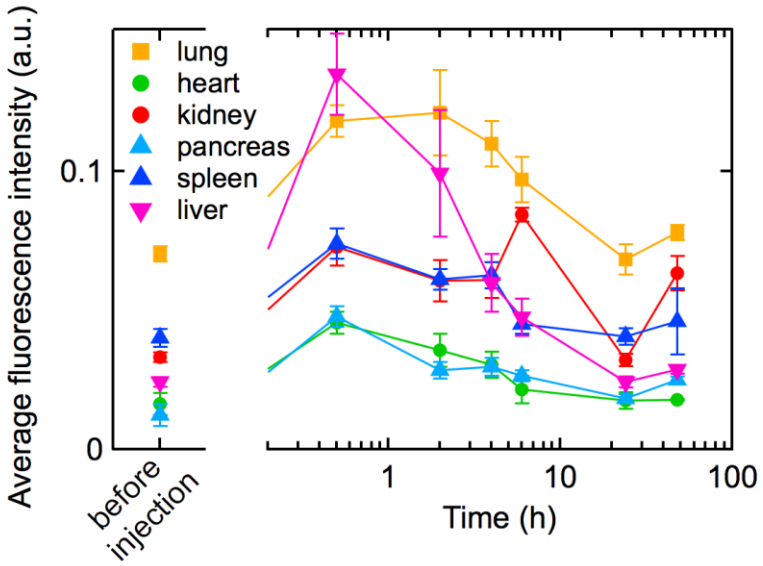

Figure 2.9 Average fluorescence intensity per pixel for different organs versus time after injection of for lipid coated $CuIn_xSe_y/ZnS$ QDs. Organs were resected and imaged using the Li-cor imaging system. Each point is the average obtained from 5 - 6 mice, except for 48 h (3 mice).

2.3.9 Biodistribution of $CuIn_xSe_y/ZnS$ QDs

Biodistribution and circulation of QDs were also studied. After each time point, mice were sacrificed and seven organs were collected. Also, their urine and feces were collected using mice urine/feces collector. Amount of In were measured by ICP-MS then compared to initial In amount. After 24 hours of injection, most of QDs were cleared out by feces and little portion were left in spleen and liver (**Figure 2.10**). QDs were circulated throughout the whole body at first, then started to clear out and only small portion were left in spleen and liver after 48 hours (**Figure 2.11**).

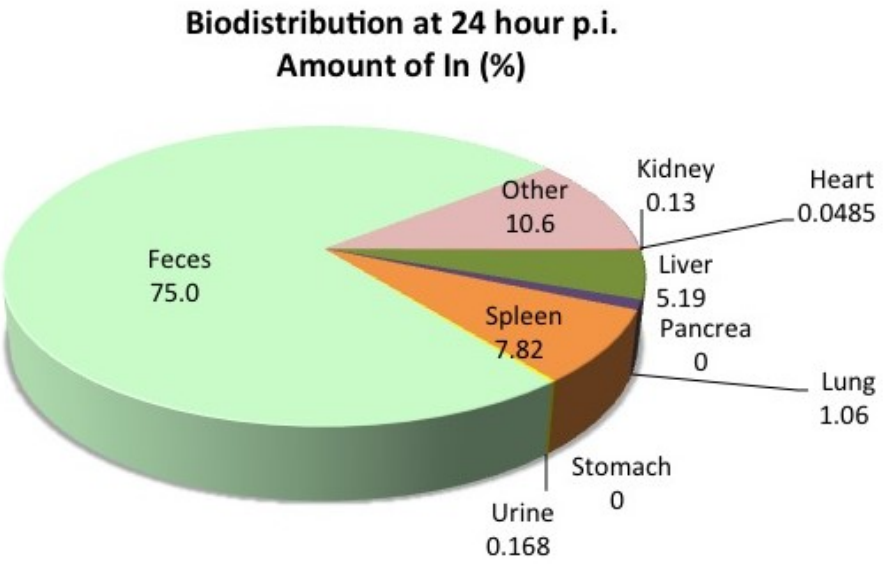

Figure 2.10 Biodistribution of lipid coated $CuIn_xSe_y/ZnS$ QDs after 24 hour post injection. The amount of In was measured by ICP-MS. The amount in urine, feces, and seven different organs were investigated. About 75% of initial amount seemed to be excreted via feces at 24 hour p.i. and small portion were left in spleen and liver.

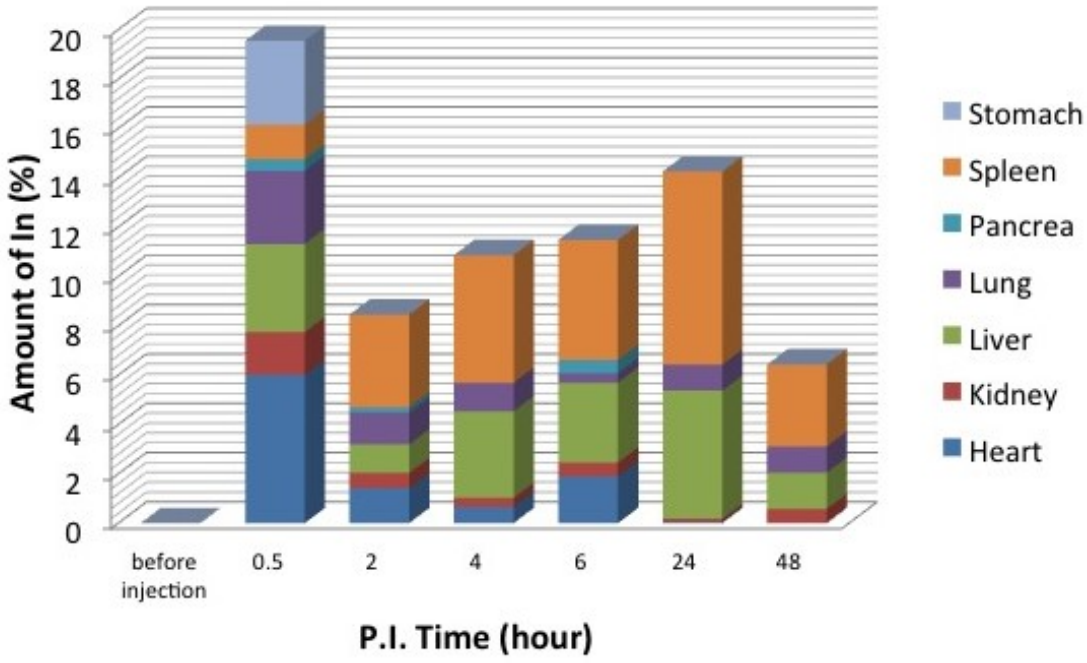

Figure 2.11 Circulation of lipid coated $CuIn_xSe_y/ZnS$ QDs at different time points (post injection). Amount of an element In was measured by ICP-MS. The amount in seven different organs (including RES system) at each time point was investigated. Most QDs circulate throughout the whole body at first and only 20% of initial amount seemed to accumulate in organs, then, they are cleared out and small portion are left in spleen and liver after 2 days.

2.3.10 Circulation of $CuIn_xSe_y/ZnS$ QDs

The kinetics of circulation were analyzed quantitatively by determining the average intensity per pixel over the whole image (**Figure 2.8e**). The average intensity remains constant for about 2 hours p.i. and then decreases to the background level before injection after 48 hours. By fitting the data to the function:

$$\frac{I(t)-I_{background}}{I_{max}-I_{background}}=\frac{1}{1+\exp\left(\frac{t-t_{1/2}}{\tau}\right)}$$

we obtain an average retention time $t_{1/2}$ of 268 ± 16 mins and a clearance time τ of 74.5 ± 11.9 mins.

These QDs are externally similar to the high density lipoprotein (HDL) particles in the body that carry cholesterol to the liver for clearance. HDL particles are lipid coated particles with diameter in the range from 10 – 15 nm and circulate freely in the body. As a result of these unique properties, modified natural HDL particles and biomimetic HDL particles have been explored as contrast agents for MRI.[106] Thus we hypothesize that the good circulation characteristics are due to the size and lipid coating.

2.4 Conclusions

In summary, we have demonstrated a novel one-pot synthesis of $CuIn_xSe_y/ZnS$ QDs with emission in the near IR, high quantum yield, and good stability. The synthesis is relatively straightforward and reproducible, and avoids the use of elements such as Cd and As. We also have demonstrated that lipid coated $CuIn_xSe_y/ZnS$ QDs are good candidates for *in vivo* imaging.

Chapter 3. Non-invasive *in vitro* cancer genomic biomarker monitoring platform

3.1 Introduction

Prostate cancer is the second leading cause of cancer death in men in the USA.[7,107,108] Measurement of serum prostate-specific antigen (PSA), the representative biomarker for prostate cancer, is a commonly used method for diagnosing and screening prostate cancer.[108-110] Every year about 10 million men in the US will have a PSA test. About 1 million of these individuals will have a positive PSA test and will undergo a biopsy.[11,19-24] Of the 1 million biopsies, about 180,000 (less than 20%) will be diagnosed with prostate cancer. The 60,000 individuals diagnosed with low grade cancer will usually undergo active surveillance, while the 120,000 individuals with intermediate, high grade, or metastatic disease will require treatment.[39,111] Performing 10 million PSA tests and 1 million biopsies to identify 120,000 individuals requiring treatment is expensive and inefficient. In addition, PSA concentration reaches almost to zero level in urine of patient after hormone therapy and PSA-based screening method alone is insufficient to provide information on genetic diversity. Therefore, there is a major need to develop diagnostic tools to identify individuals with intermediate, high grade, and metastatic disease, and the discovery of additional biomarker that supplements PSA to gain information on genetic diversity is also required.[112,113]

The widely-used PSA test has a high rate of false positives (66-76%) and false negatives (15%), leading to over-diagnosis and a large number of unnecessary biopsies.[11,19-24] Variations of the PSA test, including the Prostate

Health Index (PHI)[35,36,38,39] and 4k score[37], represent improvements, but have not enabled reliable diagnosis of prostate cancer.

More recently, expression of genomic biomarkers, such as PCA3 and fusion genes,[114] have been found to be correlated to some forms of prostate cancer.[40-45,115,116] However, very few markers are prostate cancer specific and hence a panel of biomarkers will be needed to improve sensitivity and specificity.[44,51] Based on recent results in the literature[117-119] we have identified a panel of three genes (AMACR, PCA3, and PSMA) with the potential to provide high sensitivity and specificity for diagnosis of prostate cancer.

Also, fusion genes have been regarded as both a diagnostic tool that can be used to monitor patients and therapeutic targets that will be subject to eventual treatment.[63] Gene fusion occurs in various diseases including leukemia, sarcoma, and carcinoma through chromosomal rearrangement.[64] The rearrangement of genes causes a genomic instability in cells, which results in an increased risk for the disease.[63] The prostate cancer overexpresses a specific fusion gene, *TMPRSS2-ERG*, which has a role in tumor progression including invasion and metastasis.[65] *TMPRSS2-ERG* fusions are the most predominant isoform, with multiple studies showing that approximately 50% of prostate cancers from PSA screened surgical cohorts are *TMPRSS2–ERG* fusion-positive, and greater than 90% of prostate cancers over-expressing ERG harbor *TMPRSS2–ERG* fusions.[48,66] Since the fusion gene type depends on the phase of prostate cancer progression,[66] we focused on three different target fusion genes, which fuse different regions of exon 1 or 2 of *TMPRSS2* to exon 2 or 4 of *ERG*, to achieve diagnosis of a specific phase of prostate cancer. Moreover, determination of fusion gene types in early stage cancers is important for patient therapy and prognosis.[120] Thus, we

detected fusion genes in urine samples of patient group with early stage cancer (Gleason score 6 or 7). We adopted a bio-barcode assay to increase the specificity of targeting fusion genes as well as decreasing the non-specific signal from urinary components. Importantly, we demonstrated a successful differential detection of multiple types of fusion genes from urine of patients whose PSA levels are similar. These findings suggest that differential determination of fusion genes from clinical samples can offer new insight into disease progression and clinical outcome.

Current methods for the detection of fusion genes are reverse transcription-polymerase chain reaction (RT-PCR), fluorescent in situ hybridization (FISH) and prior-cDNA microarray.[66] These methods, however, are not cost-effective and inapplicable for multiplexed detection of genes. For these reasons, interest in a new method with high sensitivity and multiplex capability has been increased recently.[121,122] A nanomaterial-based bioassay[123], a bio-barcode assay, was established that detects proteins and nucleotides with ultrahigh sensitivity.[124-126] Sandwich assay used in this technique allows an exclusive sorting of fusion genes since different sequences on each side are required to contribute to final outcome.[126-129] The sandwich assay using nanoparticles and gel electrophoresis can be easily used in any laboratory environment since it does not require large scale expensive equipment.

In this study we optimized an oligo-sandwich assay to determine the expression levels of different target genes (three different types of fusion genes, AMACR, PCA3, and PSMA). The assay uses magnetic beads (MBs) conjugated with a complementary oligo for capture, and gold nanoparticles (AuNPs) for detection, enabling easy RNA separation and multiplexing (**Figure 3.1**). Also, we suggest high throughput electrophoresis-based bio-barcode assay that can function as a model method to

determine three different types of fusion genes, AMACR, PCA3, and PSMA in urine of men with prostate cancer.

3.2 Materials and methods

3.2.1 AuNPs and barcode oligos conjugation

Thiol terminated barcode oligonucleotides were specifically designed and synthesized for its purpose (IDT). They were reduced by 100 mM 1,4-dithiothreitol (DTT, H7033, Sigma-Aldrich). By filtration using illustra™ NAP™-5 columns (GE17-0853-01, Sigma-Aldrich), barcode oligonucleotides were purified and mixed with 50 nm gold nanoparticle (AuNP, EM.GC50, BBI solutions). 10 % sodium dodecylsulfate solution (V6551, Progmega) and pH 7 phosphate buffer were added prior to eight aliquots of 2 M sodium chloride solution (S7653, Sigma-Aldrich). After completion of salt aging (final concentration of 0.3 M), the final solution was centrifuged at 12,000 rpm for 15 minutes. Pellets were re-dispersed in DI-water. A number of barcode oligonucleotides was controlled by varying the final salt concentration (0.1 and 0.5 M). Also different length of barcode oligonucleotides were used to distinguish different targets in gel electrophoresis.

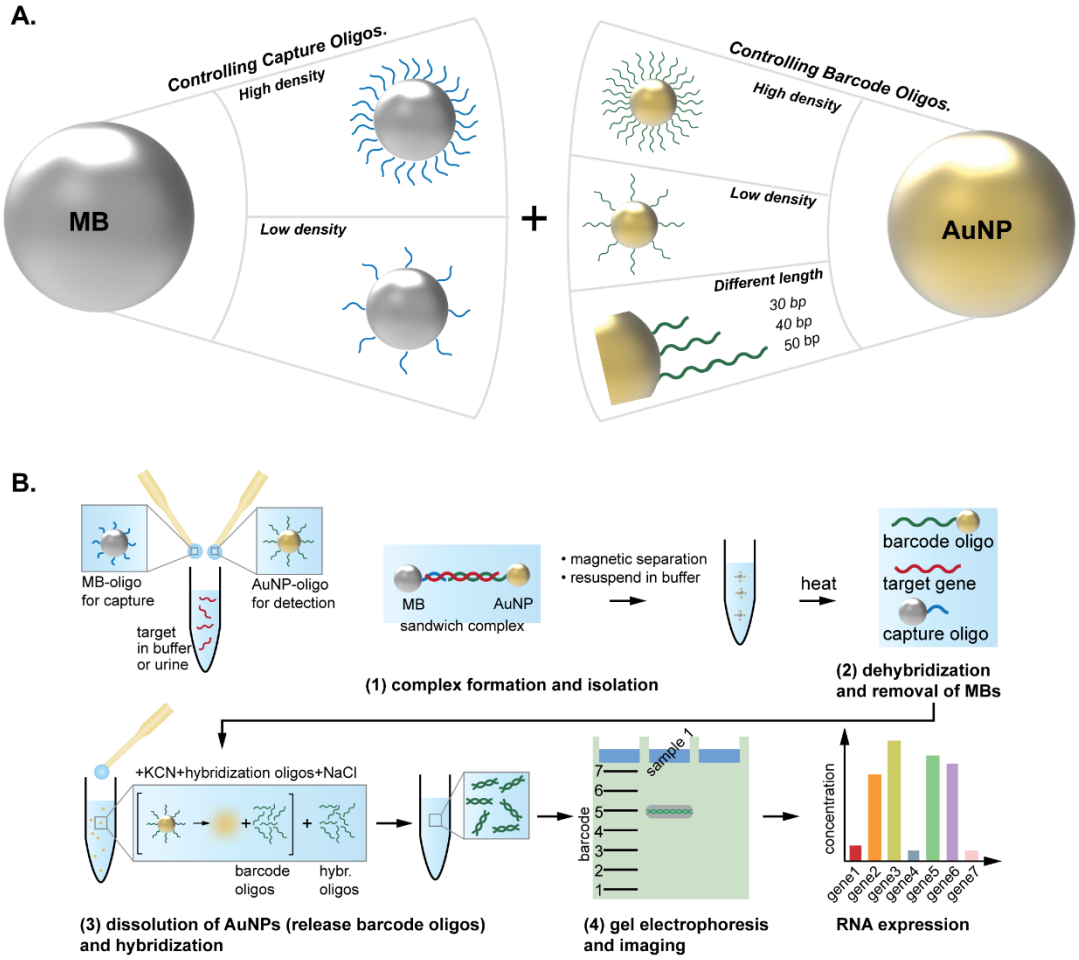

Figure 3.1 Schematic view of oligonucleotide sandwich assay using magnetic beads and gold nanoparticles.

3.2.2 Magnetic beads (MBs) and capture oligos conjugation

2.8-μm carboxylic acid-functionalized MB (Dynabeads® M-270 Carboxylic Acid, 14305D, Invitrogen, Carlsbad, California, USA) were vortexed briefly and magnetically separated in a magnetic separation rack (MSR1000, OZ Biosciences, San Diego, California, USA) for 2 minutes to remove the supernatant. The MB were then washed twice with 25 mM 2-(N-morpholino)ethanesulfonic acid (MES) (M8250, Sigma-Aldrich, St. Louis, Missouri, USA) buffer with pH 5. Amine-terminated DNA (capture DNA) (Integrated DNA Technologies, Coralville, Iowa, USA), which enabled the capturing of a target sequence as the binding to a half of the

complementary target sequence, were prepared in a MES buffer, mixed with MB and shaked at room temperature for 30 minutes.

The capture DNA and the MB were cross-linked with each other by adding 100 mg/ml N-(3-Dimethylaminopropyl)-N'-ethylcarbo-diimide hydrochloride (EDC) (03450, Sigma-Aldrich) at room temperature. After 3 hours of shaking and magnetic separation, the supernatant was removed, and the absorbance of the supernatant was then measured using UV-Vis spectrophotometer (S-3100, SCINCO, Seoul, South Korea) at 260-nm wavelength to calculate the amount of the capture DNA conjugated to MB. The MB were washed with 50 mM Tris-HCl buffer adjusted to pH 7.4 (15568-025, Invitrogen, Carlsbad, California, USA) by 10 minutes of shaking, and this washing step was repeated 2 times. Finally, DNA-functionalized MB were resuspended in phosphate-buffered saline (PBS) with pH 7.4 (10010-023, Invitrogen, Carlsbad, California, USA) at a final concentration of 30 mg/ml.

3.2.3 Quantification of the barcode oligos conjugated to AuNP

To quantify oligonucleotides fluorescently, barcode DNA modified with Alexa Fluor-488 fluorophore (Integrated DNA Technologies) were used. The procedure of preparation of fluorophore-labeled barcode DNA-modified AuNP is same as the procedure described above, except for the protection from the light to prevent photobleaching of the fluorophore. The fluorophore-labeled barcode DNA-functionalized AuNP were centrifuged at 8,500 rpm for 15 minutes and resuspended in 1 ml of deionized water to remove unbound DNA (repeated twice). After additional centrifugation, the pellet of fluorescence-labeled AuNP probes was treated with 50 μl of 25 mM potassium cyanide (KCN) (60178, Sigma-Aldrich), and the mixture was then incubated at room temperature until the entire dissolution of AuNP. Fluorescence

intensity of Alexa Fluor-488 fluorophore-modified barcode DNA was measured using Infinite® F200 Pro (Tecan, Zürich, Switzerland) to obtain the standard curve. The samples were serially diluted in 10-fold increments ranging from 10 μM to 1 nM. Finally, fluorescence intensity of the fluorescence-labeled DNA released from AuNP was measured to determine the number of barcode DNA cross-linked to AuNP by comparison to the standard curve.

3.2.4 Quantification of the capture oligos on MB

Prior to washing step with TRIS-HCl buffer solution, first supernatant were stored and absorbance at 260 nm wavelength were measured using UV-Vis spectrophotometer (3100, SCINCO). Amount of unbound capturing oligonucleotides were calculated from the absorbance measurement.

3.2.5 Sandwich assay in buffer and urine

(1) Complex formation and isolation. Prepared MBs and AuNPs (10 μL each) were mixed with different concentrations of one of the target genes (0 M, 1 fM, 10 fM, 100 fM, 1 pM, 10 pM, 100 pM, and 1 nM) in buffer or human urine **(xx, Lee Biosolution)**. First, the solution with concentration of 1 nM was made and serial dilution was performed to make 7 different concentrations. In order to minimize propagating any errors when using serial dilution, ten times larger volume (~ 1 ml) was used to make dilution. In addition, a number of target genes in each dilution can be measured via UV absorbance spectroscopy if needed. The mixture of MPs, AuNPs, and target genes was vortexed and incubated at 95 °C for 5 minutes. The ratio of AuNPs to MPs was around 225, which is optimized to assure enough space between AuNPs for minimizing steric hindrance. The

solution was then cooled to room temperature and mixed vigorously for at least 1 hour to form sandwich conjugates. The MB-AuNP conjugates were isolated from unbound AuNPs by magnetic separation.

(2) Dehybridization and removal of MBs. The AuNPs were then detached from the MP-AuNP conjugates by heating to 95 °C for 5 minutes and using magnetic separation. At this temperature, supernatant was then collected into small PCR tubes.

(3) Dissolution of AuNPs and hybridization. The solution containing the AuNPs and conjugated barcode oligos was incubated in 2 μL of 100mM potassium cyanide and 1 μL of 1 μM complementary oligonucleotides (Hyb oligo). The solution was heated to 95 °C for 5 minutes to completely dissolve the AuNPs. After incubation, the solution was cooled to room temperature to hybridize the barcode oliogs and hybridization oligos.

(4) Gel electrophoresis and imaging. A 15% acrylamide gel was prepared with a mixture of water, TBE, APS, and TEMED. The final products from the oligo-sandwich assay were mixed with 10x loading buffer and electrophoresis was performed at 120 V for 70 minutes. The gel was stained with SYBR® Green I Nucleic Acid Stain (50513, Lonza, Basel, Switzerland) enabling visualization of double-stranded DNA. Image was captured using gel documentation system (Scinomics, Daejeon, South Korea).

3.2.6 Collection of urine specimens from prostate cancer patients

Noninstrumented voided urine samples were obtained from 14 patients with informed consent before and after a digital rectal examination (DRE) at the ASAN

Medical Center (AMC). Urine collection cups containing RNA preservative (RNAlater, 76104, QIAGEN, Hilden, Germany) and antibiotics (15240-062, Invitrogen, Carlsbad, California, USA) were used to obtain urine from each subject after DRE was performed by the practicing urologist.

3.2.7 Sandwich assay with clinical samples

In the tests for clinical urine samples, an RNase-free environment was maintained during RNA isolation and reaction procedure. Target nucleotide enrichment was performed using 15 μl of MB probes on each urine specimen with incubation at room temperature for 1 hour. After the incubation, MB-target complexes were washed twice with hybrid buffer and resuspended in 100 μl of hybrid buffer. The target-capturing MB probes were used for the assay as in the same method described above.

Figure 3.2 illustrates key detection steps for multiple fusion genes in prostate cancer using patient urine. The magnetic probes form sandwich complexes with AuNP probes through complementary hybridization with target fusion genes. Before gel electrophoresis, the barcode DNA was released from AuNP by dissolving the AuNP core using KCN. In the final step, we added complementary sequences to the barcode DNA to make dsDNA, since the dye molecule, SYBR Green I, for staining DNA could be intercalated into dsDNA. This dsDNA was separated during electrophoresis by their different molecular weights (barcode I, 9193.1 g/mole; barcode II, 12667.5 g/mole; barcode III, 18444 g/mole), that is the main force for the capability for multiplexed detection in a single gel.

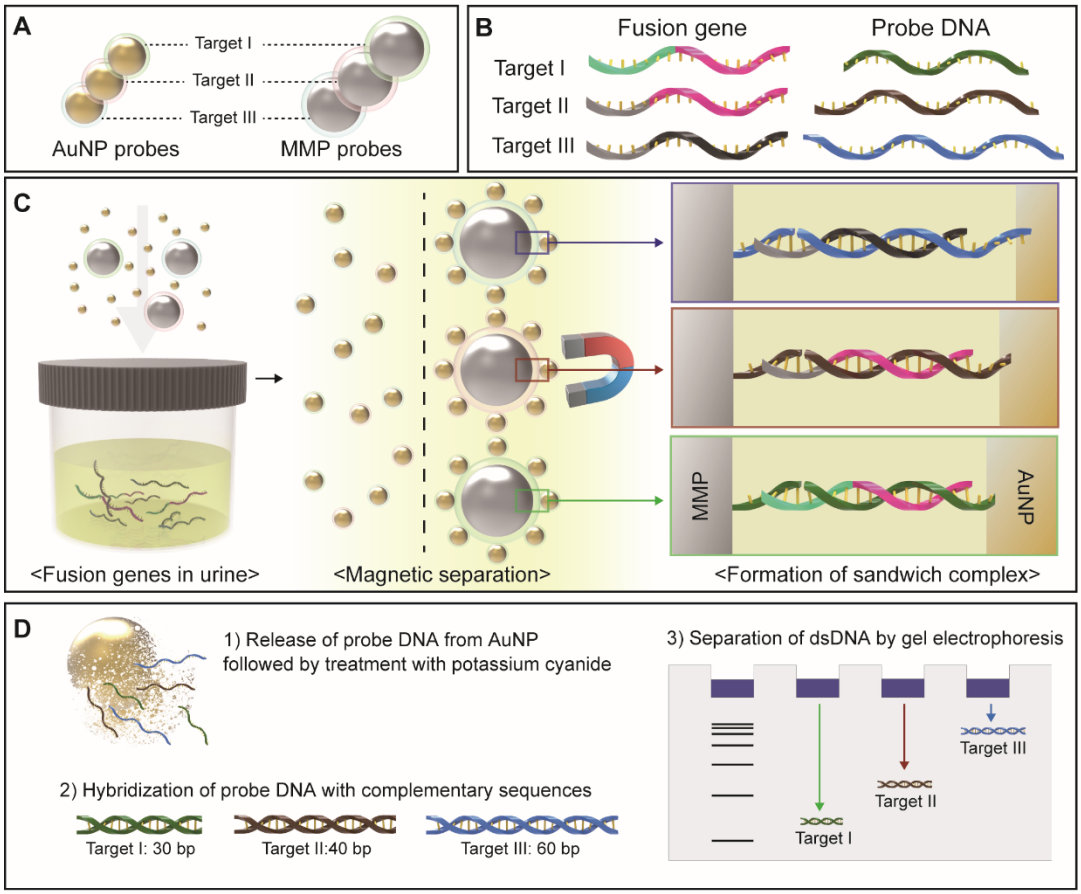

Figure 3.2 Schematic view of oligonucleotide sandwich assay using magnetic beads and gold nanoparticles in patient's urine sample

3.3 Results and Discussion

3.3.1 Design of oligonucleotides

Barcode and capture oligos are designed to form complementary pairs with each target gene (GenBank#: AMACR: AF047020.1, PCA3: AF103907, PSMA: NM_001193472.1). Both oligos contain ten A-spacers at one end to enable conjugation on the surface of the nanoparticles and hence exposing the hybridizing portion of the sequences towards the outside. Capture oligos contain an amine group at the end of sequences to enable amide conjugation to the carboxyl group on the magnetic beads. The barcode oligos contain a dithiol group which enables binding to the surface of the AuNPs after reduction. The barcode oligos used for quantification are composed of the same sequences with the addition of a fluorescent dye (I6-FAMK: Abs 496 nm, Em 516 nm), inserted at the end of the sequences. Three different lengths of barcode oligos were prepared (30 base pairs for AMACR, 40 for PCA3, and 50 for PSMA) to distinguish the three different target genes in gel electrophoresis (**Figure 3.1**). Hybridization oligos were designed to complement the barcode oligos. The full sequences of all oligonucleotides are provided in supplementary information (**Table 3.1**). Chromosomal rearrangement occurs at various point of exons that results in different lengths and compositions of *TMPRSS2-ERG* fusion genes. Such fusion genes exacerbate the genetic diversity leading to the prostate cancer. For this reason, we selected three types of fusion genes [Target I, *TMPRSS2* Exon 1 and 2 (Tm1/2) + *ERG* Exon4 (E4); Target II, Tm1 + E4; Target III, Tm1 + E2] that express high frequency in prostate cancer.[66] Target II, found in 86 % of cases, has been reported as the most common isoform in prostate cancer. Although target I (26%) and III (20%) are expressed less than target II, they represent severe

clinical outcomes because of seminal vesicle invasions in patients.[66]

AMACR target	CAGGGCATCTCGGTCATGGAGCTGTCCGGCCTGGCCCCGGGCCCGTTCTGTGCTATGGTCCTGGCT GACTTCGGGGCGCGTGTGGTACGCGTGGACCGGCCCGGCTCCCGCTACGACGTGAGCCGCTTGGG CCGGGGCAAGCGCTCGCTAGTGCTGGACCTGAAGCAGCCGCGGGGAGCCGCCGTGCTGCGGCGT CTGTGCAAGCGGTCGGATGTGCTGCTGGAGCCCTTCCGCCGCGGTGTCATGGAGAAACTCCAGCTG GGCCCAGAGATTCTGCAGCGGGAAAATCCAAGGCTTATTTATGCCAGGCTGAGTGGATTTGGCCAGT CAGGAAGCTTCTGCCGGTTAGCTGGCCACGATATCAACTATTTGGCTTTGTCAG
PCA3 target	ACAGAAGAAATAGCAAGTGCCGAGAAGCTGGCATCAGAAAAACAGAGGGGAGATTTGTGTGGCTG CAGCCGAGGGAGACCAGGAAGATCTGCATGGTGGGAAGGACCTGATGATACAGAGGAATTACAAC ACATATACTTAGTGTTTCAATGAACACCAAGATAAATAAGTGAAGAGCTAGTCCGCTGTGAGTCTCCT CAGTGACACAGGGCTGGATCACCATCGACGGCACTTTCTGAGTACTCAGTGCAGCAAAGAAAGACT ACAGACATCTCAATGGCAGGGGTGAGAAATAAGAAAGGCTGCTGACTTTACCATCTGAGGCCACAC ATCTGCTGAAATGGAGATAA
PSMA target	CAGTGCACTCTAGAAACACTGCTGTGGTGGAGAAACTGGACCCCAGGTCTGGAGCGAATTCCAGCC TGCAGGGCTGATAAGCGAGGCATTAGTGAGATTGAGAGAGACTTTACCCCGCCGTGGTGGTTGGAG GGCGCGCAGTAGAGCAGCAGCACAGGCGCGGGTCCCGGGAGGCCGGCTCTGCTCGCGCCGAGAT GTGGAATCTCCTTCACGAAACCGACTCGGCTGTGGCCACCGCGCGCCGCCCGCGCTGGCTGTGCGC TGGGGCGCTGGTGCTGGCGGGTGGCTTCTTTCTCCTCGGCTTCCTCTTCGGTTAAAAGCCAACTGCA AGGTCTAATGACTGCA
AMACR target short version	CCTGGCCCCG GGCCCGTTCT GTGCTATGGT CCTGGCTGAC
PCA3 target short version	AAGCTGGCAT CAGAAAAACA GAGGGGAGAT TTGTGTGGCTG CAGCCGAGGG
PSMA target short version	TGCACTCTAG AAACACTGCT GTGGTGGAGA AACTGGACCC CAGGTCTGGA GCGAATTCCA
AMACR capture oligo	AGAACGGGCC CGGGGCCAGG AAAAAAAAAA/NH2/
PCA3 capture oligo	TGTTTTTCTG ATGCCAGCTT AAAAAAAAAA/NH2/
PSMA capture oligo	AGCAGTGTTT CTAGAGTGCA AAAAAAAAAA/NH2/
AMACR barcode oligo	/S-S/AAAAAAAAAA GTCAGCCAGG ACCATAGCAC
PCA3 barcode oligo	/S-S/AAAAAAAAAA CCCTCGGCTG CAGCCACACAA ATCTCCCCTC
PSMA barcode oligo	/S-S/AAAAAAAAAA TGGAATTCGC TCCAGACCTG GGGTCCAGTT TCTCCACCAC
AMACR barcode fluorophore oligo	/5ThioMC6-D//i6-FAMK/AAAAAAAAAA GTCAGCCAGG ACCATAGCAC
PCA3 barcode fluorophore oligo	/5ThioMC6-D//i6-FAMK/AAAAAAAAAA CCCTCGGCTG CAGCCACACAA ATCTCCCCTC
PSMA barcode fluorophore oligo	/5ThioMC6-D//i6-FAMK/AAAAAAAAAA TGGAATTCGC TCCAGACCTG GGGTCCAGTT TCTCCACCAC
AMACR hyb oligo	GTGCTATGGT CCTGGCTGAC TTTTTTTTTT
PCA3 hyb oligo	GAGGGGAGAT TTGTGTGGCTG CAGCCGAGGG TTTTTTTTTT
PSMA hyb oligo	GTGGTGGAGA AACTGGACCC CAGGTCTGGA GCGAATTCCA TTTTTTTTTT
PCA3 target 10 bp overlapping	GGTGGGAAGG ACCTGATGAT AC
PCA3 capture oligo 10 bp overlapping	CCTTCCCACC AAAAAAAAAA/NH2/
PCA3 barcode oligo 10 bp overlapping	/S-S/AAAAAAAAAA TTCATTGAAA CACTAAGTAT ATGTGTTGTA ATTCCTCTGT ATCATCAGGT
PCA3 hyb oligo 10 bp overlapping	ACCTGATGAT ACAGAGGAAT TACAACACAT ATACTTAGTG TTTCAATGAA TTTTTTTTTT

Table 3.1. The sequence information of three targets (AMACR, PCA3, PSMA); red letters indicate the complementary region between target and capture oligos, blue letters indicate the complementary region between target and barcode oligos. Yellow letters indicate portion of hyb oligos that forms complementary pair with barcode oligos.

Name	Sequence (5′ ---------- 3′)
Target I	GATGGCTTTGAACTCA/GAAGCCTTAT
Target II	GAGCGCGCAG/GAAGCCTTAT
Target III	GCCTGGAGCGCGGCAG/GTTATTCCAG
MB I	TGAGTTCAAAGCCATCAAAAAAAAAA/NH_2/
MB II	CTGCGCGCTCAAAAAAAAAA/NH_2/
MB III	CTGCCGCGCTCCAGGCAAAAAAAAAA/NH_2/
Probe I	/S-S/AAAAAAAAAACTCACAACTGATAAGGCTTC
Probe II	/S-S/AAAAAAAAAAGGGCTGATCCCTGACAACTGATAAGGCTTC
Probe III	/S-S/AAAAAAAAAAGCTTTTGGTCAACACGGC TTTCCTCGGGTCTCCAAAGATCCTGGAATAAC
Hyb I	GAAGCCTTATCAGTTGTGAGTTTTTTTTTT
Hyb II	GAAGCCTTATCAGTTGTCAGGGATCAGCCCTTTTTTTTTT
Hyb III	GTTATTCCAGGATCTTTGGAGACCCGAGGA AAGCCGTGTTGACCAAAAGCTTTTTTTTTT

Table 3.2. The sequence information of oligonucleotides. Red letters of target DNA indicate the region of *TMPRSS2* and black ones are the region of *ERG*. The blue region of MB DNA binds to red region of the target DNA. The green part of probe DNA binds to the other half region of target DNA.

To detect three target fusion genes, we designed barcode sequences based on the sequences of *TMPRSS2* (NM_005656) and *ERG* (NM_0044490) (**Table 3.2**). As contain the part of *TMPRSS2-ERG* fusion region as well as different sequence lengths, which enable the assay to detect multiple targets simultaneously through separation of barcode DNA on gel electrophoresis (**Table 3.2**). Since gold-thiol chemistry was used to conjugate the barcode DNA with AuNP,[130-132] we added the thiol group at the 5' end of barcode DNA. Additionally, we inserted a 10-base adenine sequence (poly A_{10}) next to the thiol group to reduce the steric hindrance, because poly A_{10} can provide the space via the interaction between adenine and Au.[133,134]

3.3.2 Conjugating capture oligos to MBs

The capacity for capture of target oligos was adjusted by incubating the MBs with different amounts of capture oligos (typically 3 M – 45 M per MB). The capture oligos were coupled to the MBs using standard EDC chemistry. After 4 hours of conjugation, the unbound capture oligos remaining in the supernatant were isolated by magnetic separation. The amount of conjugated capture oligos was then calculated from the total concentration and the amount of unconjugated oligos measured from absorbance. The number of the capture oligos per MB increased monotonically for all three genes from 800,000 (1 nmol of oligos) to 12 million (15 nmol of oligos) (**Figure 3.3A** & **Table 3.3)**. In all cases, the amount of conjugated oligos was around 25% of the initial concentration. These results show that the conjugation efficiency was constant and that the initial

concentration is the dominant factor in controlling the number of conjugated oligos per MB.

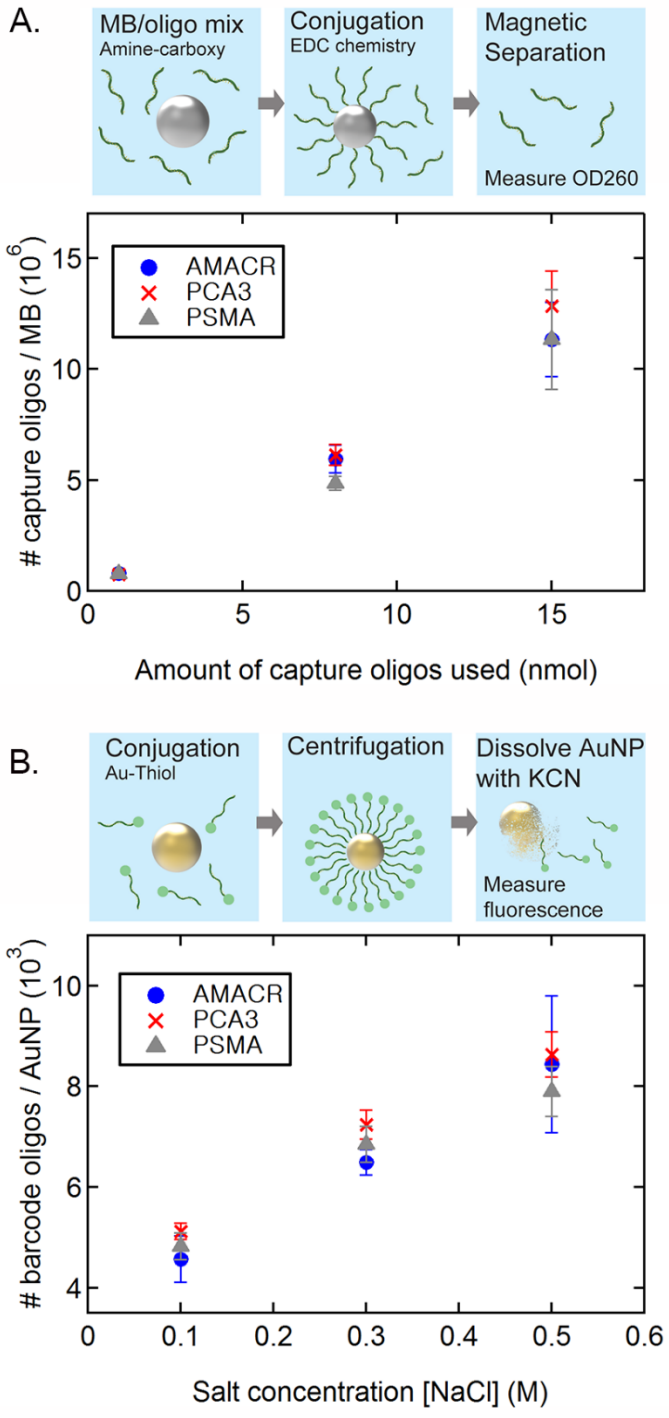

Figure 3.3. Controlling the number of capture and barcode oligonucleotides. (A) The amount of capture oligos on the MBs increased monotonically with the

initial concentration. (B) Different amount of barcode oligos on AuNP were prepared by controlling final salt concentration during salt again process.

2.8-μm carboxylated-magnetic MB was used to capture target genes specifically in urine solution, which led decrease in the non-specific interaction with urinary components. In addition, the total experimental time was reduced by eliminating the RNA purification step that usually takes around 90 min. Magnetic probe isolates the target bound-AuNP in assay solution. Three kinds of amine-functionalized oligonucleotides (capture sequences) that are complementary to different regions of *TMPRSS2* gene, were conjugated with MB via EDC coupling chemistry (**Table 3.2**). We quantified the amount of oligonucleotides on a MB by measuring absorbance at 260 nm and found that magnetic probes have an average number of 120,000 of amine-oligonucleotides per particle (data not shown).

Capture oligo density	# Capture oligos	Barcode oligo density	# Barcode oligos
Low	710,000	Low	4,650
Med	5,000,000	Med	6,850
High	12,100,000	High	8,500

Table 3.3. The average amount of capture oligos per MB and that of barcode-i6-FAMK per AuNP. The average value was calculated from five individual experiments.

3.3.3 Conjugating barcode oligos to AuNPs.

Barcode oligos were conjugated to the 50 nm AuNPs using a thiol group. The number of barcode oligos conjugated to the AuNPs is dependent on the number of oligos incubated with the AuNPs and the concentration of the salt solution. Incubation in salt solution results in salt-aging, a process that helps conjugation of oligos on AuNP while maintaining stability of AuNP.[133,135] Here we fixed the amount of thiolated barcode oligos incubated with the AuNPs and assessed the influence of the salt concentration during aging. Varying input amount of oligos with fixed salt concentration is very challenging and usually results in low reproducibility due to lack of control.

The number of barcode per AuNP was determined by incubating the AuNPs with fluorescently-labelled barcode oligos. Following centrifugation to separate the AuNP-barcode complexes from the unbound barcode oligos, fluorescence was used to determine the number of conjugated oligos (**Figure 3.4**). The number of barcode oligos increased from about 4,800 (48% of the initial concentration) in a 0.1 M salt concentration to about 8,300 in 0.5 M (83% of the initial concentration) (**Figure 3.3B and Table 3.3**).

Successful conjugation was confirmed by DLS measurements of the hydrodynamic diameter of the AuNPs which increased monotonically with the number of base pairs of the barcode oligos (30, 40, and 50 base pairs) (**Figure 3.5**). These results show that the final salt controls the efficiency of conjugation and enables conjugation of a desired number of barcode oligos to the AuNPs. Note that in the assay, following formation of the sandwich complex, the barcode oligos were released by dissolving AuNPs in KCN.

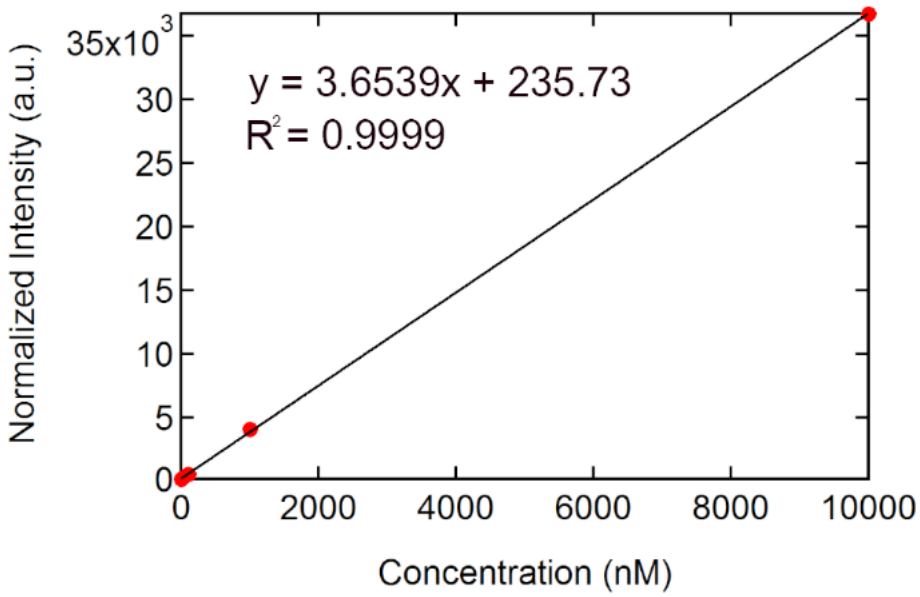

Figure 3.4. The standard curve of I6-FAMK labeled PSMA3 barcode oligos fluorescence intensity versus concentration, ranging from 10 nM 10,000 nM

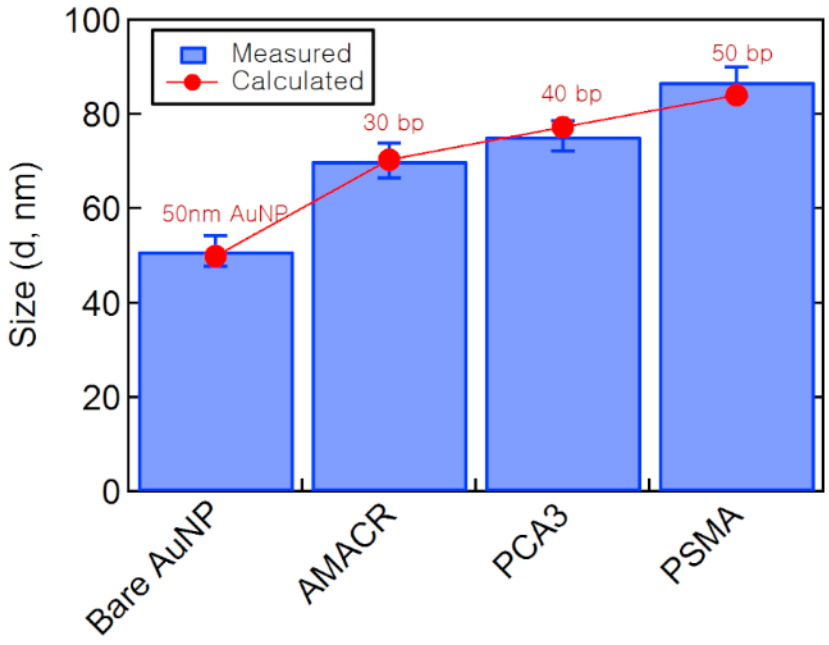

Figure 3.5. DLS measurement of bare AuNP (50nm) and barcode oligo conjugated AuNPs. Blue bar graph indicates measurement from DLS and red line represent expected size of AuNP before and after conjugation with different length of barcode oligos.

To increase the loading capacity of the AuNP, we used the salting-aging method to achieve the maximum loading of the barcode DNA through the reduction of the repulsion forces between the DNA strands.[133] To quantify the amount of barcode DNA per AuNP, we added the Alexa Fluor 488 dye onto the end of 3' for fluorescence assay. After conjugation, we dissolved the AuNP using KCN solution and then measured the fluorescence signal of barcode DNA. We found that about 1200 barcode DNA could be immobilized on 50-nm AuNP (**Figure 3.6 and Table 3.4**). Since the final signal of the assay depends on the amount of barcode DNA in gel, the functionalization of barcode DNA on the AuNP can amplify the detection signal by a factor 1000.

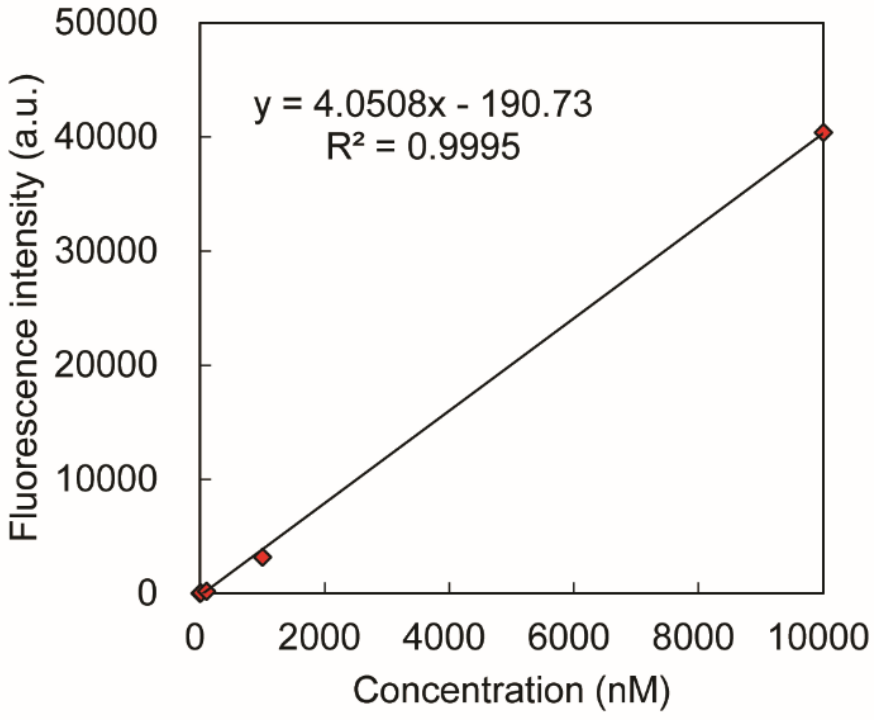

Figure 3.6. The standard curve of Alexa Fluor 488-labeled target II probe DNA fluorescence intensity versus concentration, ranging from 1 nM to 10000 nM. Deionized water was used for blank.

The average number of probe II-Alexa Fluor 488 after dissolving AuNP	1253.80 (59.30)

Table 3.4. The average amount of probe II DNA conjugated to 50-nm AuNP. Fluorescence intensity of probe II-Alexa Fluor 488 was measured after dissolving AuNP by using 100 mM KCN. 100 mM KCN solution was used for blank. The average fluorescence intensity of probe II-Alexa Fluor 488 released from AuNP was applied to the standard curve in Fig. S1, and the approximate number of conjugated probe DNA to AuNP were calculated. (n=4)

3.3.4 Influence of the number of capture and barcode oligos on the sandwich assay.

First, the effect of the number of capture oligos per MB and barcode oligos per AuNP was investigated using a three different concentrations of capture oligos (≈0.8 M, ≈6 M, and ≈ 12 M per MB) and three different concentrations of barcode oligos (≈4,000, ≈7,000, and ≈8,000 per AuNP) for the three different genes (**Figure 3.7 and 3.8**). The number of barcode oligos per AuNP represents the amplification factor of the assay, since for every AuNP that forms a complex with a target gene and MB, the barcodes on the AuNPs provide the readout in gel electrophoresis. The concentration of barcode oligos correspond to approximate area per molecule of 4 – 8 nm^2. Therefore the highest concentration may (lowest area per molecule) may result in steric hindrance of the target oligo in hybridization.

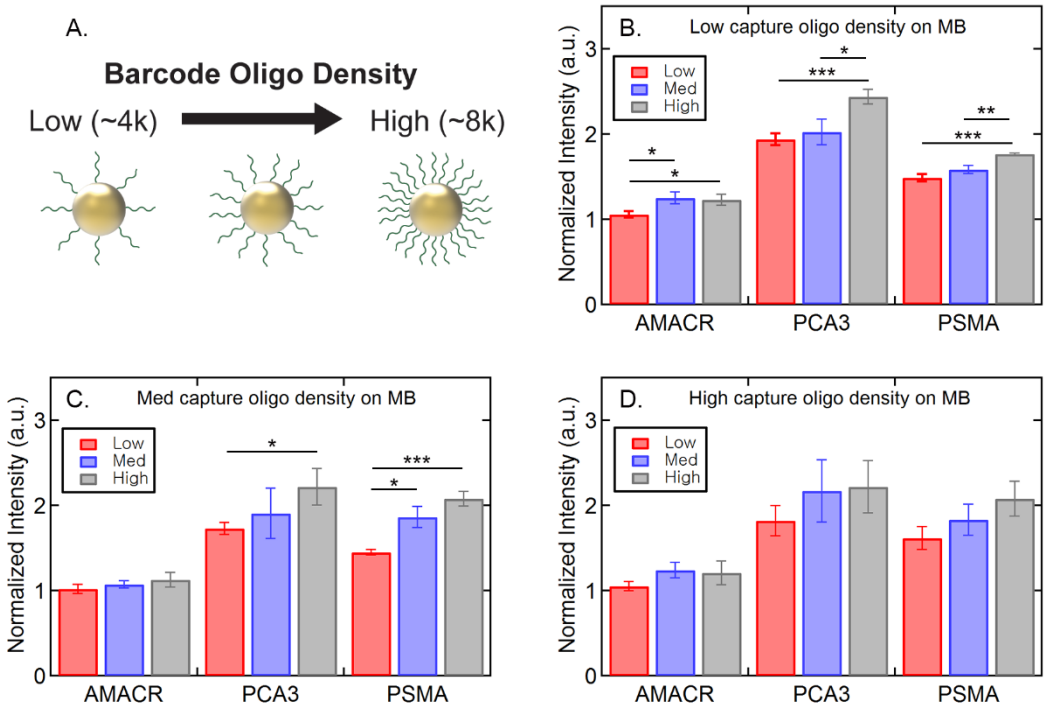

Figure 3.7. Effect of using different number of barcode oligo density (A) schematic of different barcode oligo density on AuNP. Assay results using different amount of barcode oligos on (B) low, (C) med, (D) high capture oligo density on MB. Target gene concentration was chosen to be 100 pM to be confident with the results based on supplementary Figure S2. In this test, longer versions of targets were used in order to mimic more nature form of target genes. Statistical significance was determined by Student's t-test. *$p < 0.05$, **$p < 0.01$, ***$p < 0.001$.

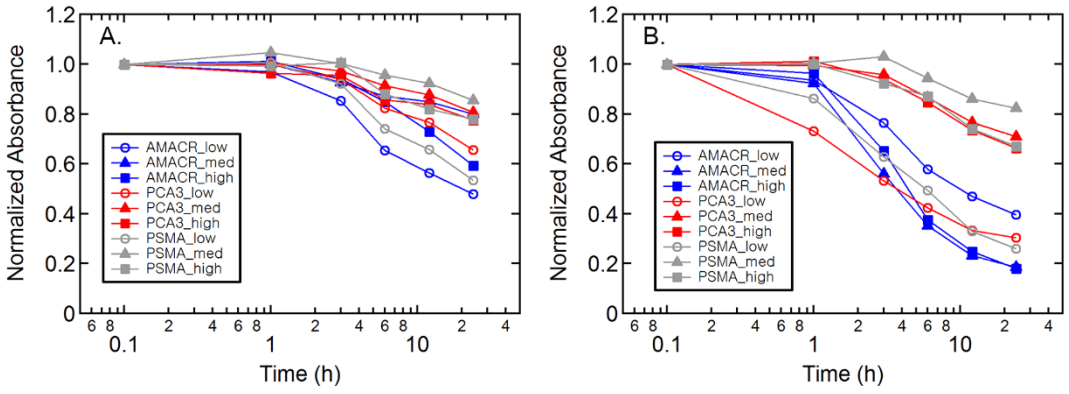

Figure 3.8. Stability of AuNPs with different amounts of barcode oligos. (A) 0.1 M NaCl, and (B) 0.3 M NaCl. (O) low oligo density (5,000 per AuNP), (Δ) medium oligo density (7,000 per AuNP), and (∂) high oligo density (8,000 per AuNP). Stability was determined from the plasmon absorbance the AuNPs at XXX nm using standard curves. (Blue) AMACR, (red), PCA3, and (gray) PSMA. AuNPs with med and high density oligos are very stable longer than the reaction time 1h in both conditions for all three types.

Experiments were performed with a target length of around 350 base pairs for all three genes to mimic the natural form and at a concentration of 100 pM to ensure tests were performed above limit of detection (LOD) of the assay (**Figure 3.9**). In these experiments, the concentration of MBs was 33 fM in mL of sample solution (2×10^7). Therefore, the theoretical detection limit (1 target per MB), corresponds to 33 attomoles (33 fM) target. The saturation limit of the assay is determined by the number of capture oligos per MB, which ranged from 26 picomoles (26 nM) at the lowest capture oligo concentration, to 393 picomoles (393 nM) at the highest capture oligo concentration.

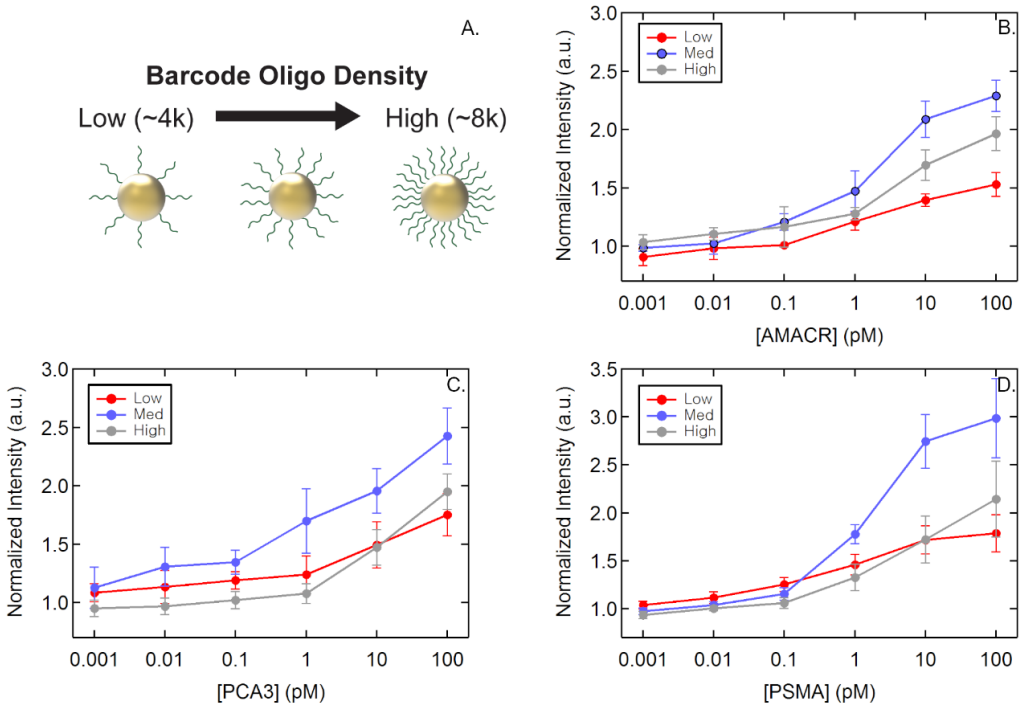

Figure 3.9. Different number of barcode oligos were used to test the effect of amount of barcode oligos Fixed number of capture oligos were used for all experiments. (B) Low density, (C) med density, (D) high density of capture oligos were used. There is no significant differences between three densities at lower concentrations, however, significant improvement was observed from 1 pM target concentration when med density barcode oligo was used.

In general, the normalized intensity of the respective bands for the three genes in gel electrophoresis increased with increasing number of barcode oligos per AuNP (**Figure 3.7**). However, it is evident that the signal does not increase proportionally with the number of barcode oligos per AuNP. This is typical for gel based detection methods due to limitation of gel imaging.[136]

Nanoparticles are very sensitive to their environment due to high surface/volume ratio. To assess their stability, AuNPs with different concentrations of barcode oligos were incubated in 0.1 M NaCl or 0.3 M NaCl. From the absorbance of the AuNPs, we found that in 0.1 M NaCl, 96% of the conjugated AuNPs remain stable for at least 1 hour, the length of the assay (**Figure 3.8A**). In 0.3 M NaCl, except for AuNPs with a low density of barcode oligos, 92% are stable for at least 1 hour (**Figure 3.8B**). This result suggests that the medium density of barcode oligos (≈7,000 per AuNP) is the minimum value to maintain stability during complex formation. Therefore, we selected 7,000 barcode oligos per AuNP to maintain stability and minimize cost and reagents.

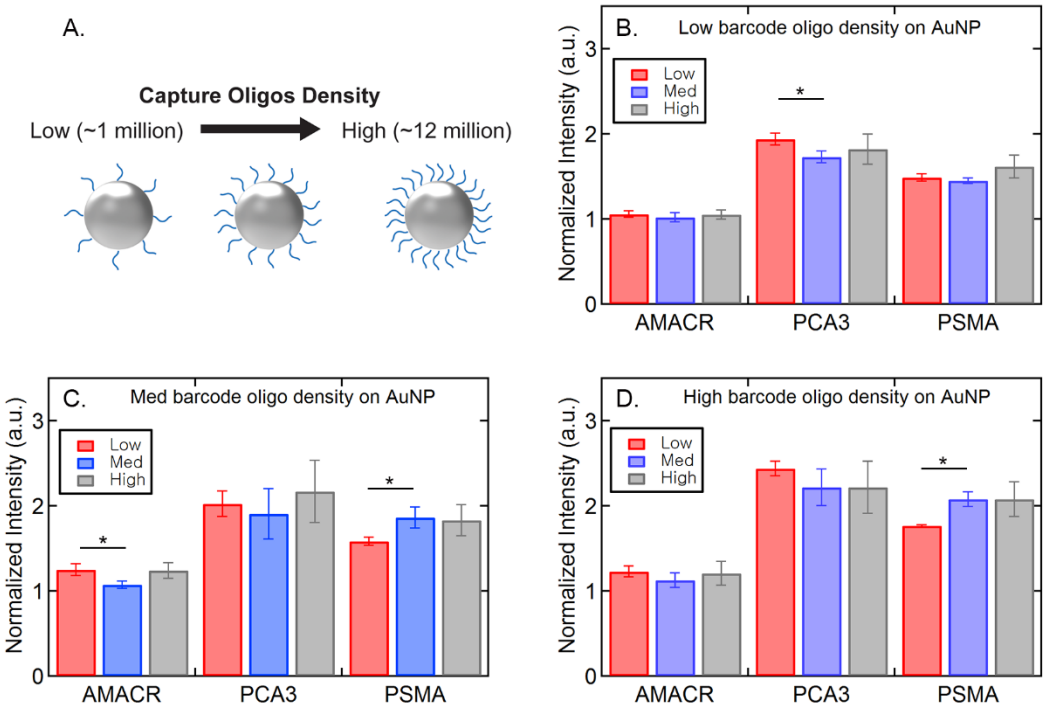

Figure 3.10. Effect of using different number of capture oligo density (A) schematic of different capture oligo density on MB. Assay results using different amount of capture oligos on (B) low, (C) med, (D) high barcode oligo density on

AuNP. Target gene concentration was chosen to be 100 pM to be confident with the final result based on supplementary data xx. In this test, longer versions of targets were used to mimic more nature form of target genes. Statistical significance was determined by Student's t-test. *$p < 0.05$.

Next, the effect of using different concentrations of capture oligos was investigated. In these experiments, the assay was performed with 3 different concentrations of capture oligos (800,000, 6,000,000, and 12,000,000 per MB) and a fixed concentration of barcode oligos per AuNP (7,000 per AuNP). Experiments were performed with 100 pM of the target gene, as described previously. The results are same as in **Figure 3.7** and replotted in **Figure 3.10**.

The assay output intensity is independent of the amount of capture oligos per MB (**Figure 3.10**). This confirms that there are sufficient capture oligos to bind the target oligos in the sample in all cases. The concentration of target oligos (100 pM = 6×10^9 oligos in the sample) is larger than the number of MBs (2×10^7), and hence above the theoretical detection limit. We note that the MBs are 2.8 μm in diameter, and hence we cannot use DLS to confirm the conjugation with the capture oligos. TEM images (Figure 3.11) might indicate that it is the efficiency of complex formation that is the limiting step. Even if there are millions of capture oligos on MB, there are hundreds of AuNPs that formed complex formation.

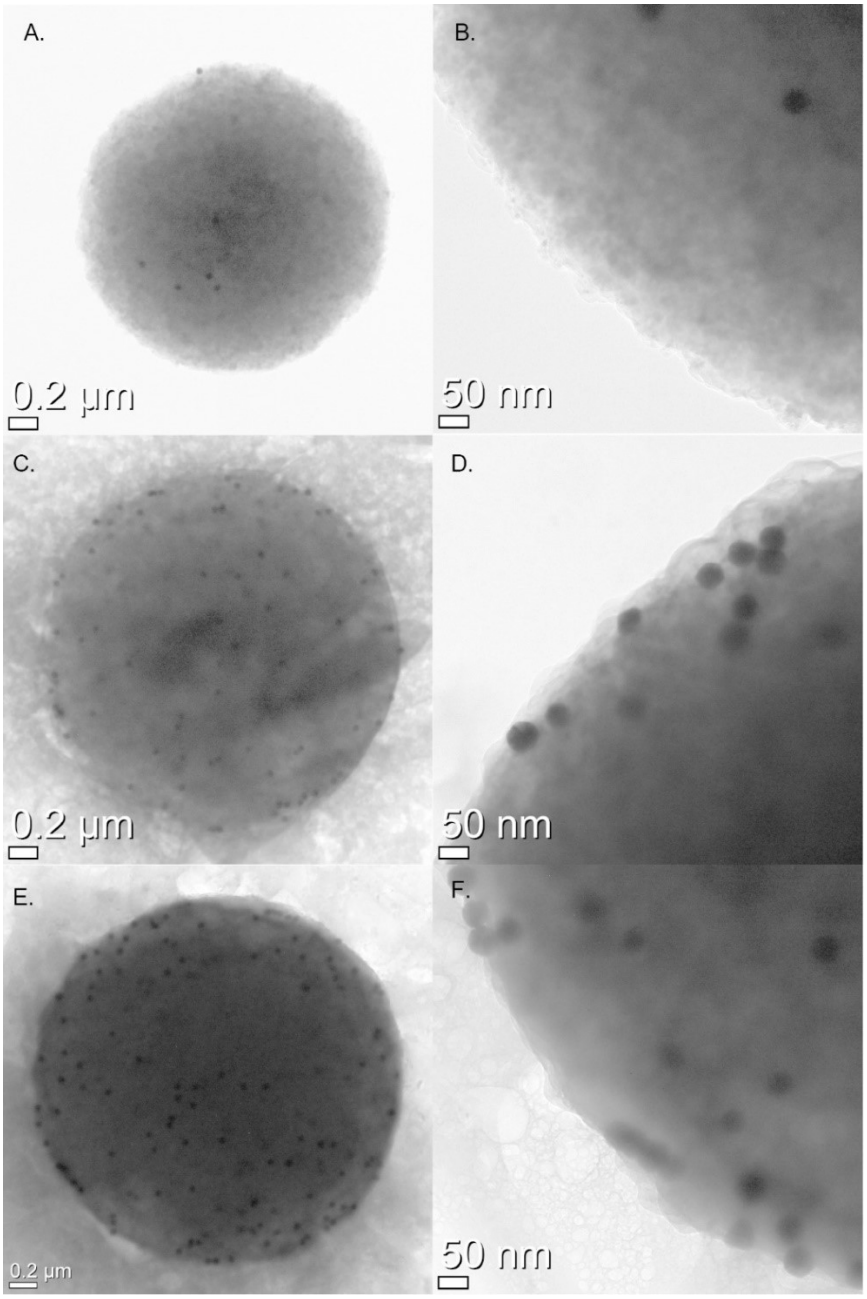

Figure 3.11. TEM images of MB-target-AuNP sandwich complex. All samples were prepared after performing the assay with different concentration of PCA3 targets (A), (B): 0, (C), (D): 1 pM, (E), (F): 100 pM. (A) and (B) show representative images of NC where no target was introduced. This indicates very little non-specific binding between MB and AuNP. AuNP/MB is 8. At higher concentrations of targets, more AuNP/MB were observed. AuNP/MB is 80 for (C) 1 pM target concentration, and 128 for (E) 100 pM target concentration.

3.3.5 The number of overlapping oligonucleotide base pairs.

Sequence design is an important parameter in sandwich assays. In addition to the sequence of the complementary pairs between targets and capture/barcode oligos, the length of the overlapping sequences was investigated. We compared assays with 10 – 30 base pair overlapping sequences for the capture/barcode oligos for hybridization with the target genes. Here we define an overlap of 10 bps as 10 bps hybridizing with the capture oligo and 10 bps hybridizing with the barcode oligo. In this experiment, a shorter version of the target genes was used to focus on the effect of the overlapping portion and minimize as many variables as possible. Longer target oligo could have secondary structure that hinder hybridization or require more time to hybridize. The sequence of the target is chosen based on previously published primer sequences used.[137]

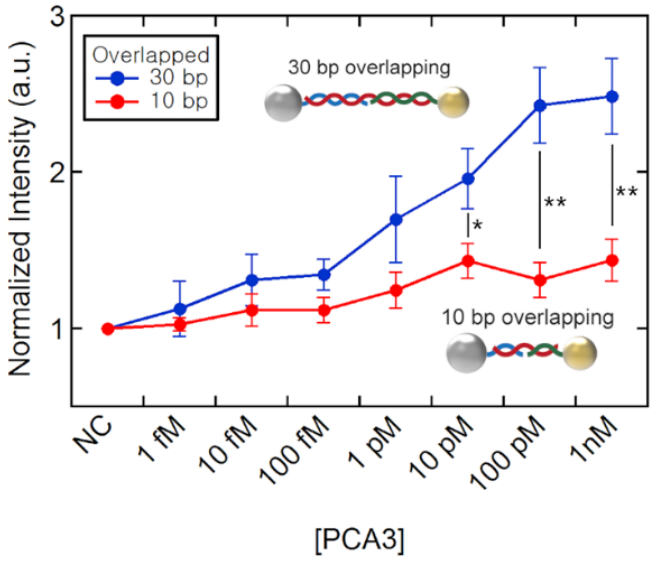

Figure 3.12. Different number of overlapped sequences between target and barcode oligos make differences in results. Assay performed with barcode oligos

that overlaps 10 bp show lower intensity compared to one with 30 bp overlapped bp. Statistical significance was determined by Student's t-test. *$p < 0.05$, **$p < 0.01$. All barcode sequences are listed in **Table 3.1**.

As a number of overlapping base pairs increased, the intensity of the bands in the assay increased (**Figure 3.12**). An overlap of 10 base pairs showed statistically significant differences from 10 pM when compared to 30 base pair overlapped sequences. Length of both overlapping base pairs between targets and oligos used for MB and AuNP play a very important role in specificity which increases the signal.

3.3.6 Single target detection (AMACR, PCA3, & PSMA) in buffer solution

Based on experiments to assess the individual steps in the assay, we determined that the optimum conditions are: 7,000 barcode oligos on the AuNPs, 6 x 10^6 capture oligos on MBs, and longer than 20 base pair overlapping sequences. To test the assay performance, targets genes were spiked into buffer solution with seven different concentrations. In all cases we used 2 x 10^7 MBs in 1 mL samples, corresponding to a detection limit (with 1 target per MB) of 33 attomoles or 33 fM of the target gene. From the number of capture oligos, the theoretical saturation limit was 200 picomoles or 200 nM of the target gene. All intensities were normalized to samples with no target gene (NC).

For all three target genes, the normalized intensity of the assay increased with target gene concentration, above a threshold (**Figure 3.13**). The limit of detection

(LOD) is the lowest concentration at which target can be detected with 95% confidence.[138,139] It was determined in the same way described in previous publication[115] using following equation.

$$\mathrm{LOD} = \mathrm{LOB} + 1.645\left(SD_{low\ concentration\ sample}\right)$$

$$\mathrm{LOD: limit\ of\ detection, LOB: limit\ of\ blank}$$

The LoD in spiked buffer was determined to be 1 pM and in spiked urine was 1-10 pM. Difference in intensity were observed in range of 0.1 - 1 pM.

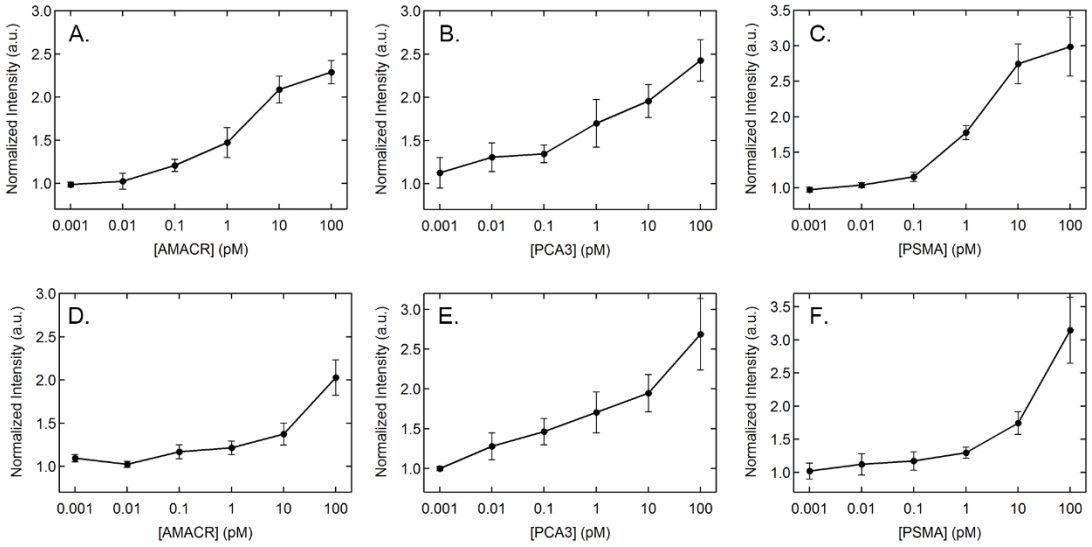

Figure 3.13. LOD of the sandwich assay was investigated. Different concentrations of three target genes, (A) AMACR, (B) PCA3, and (C) PSMA, were spiked into buffer solution. Obvious intensity difference was observed from 10~100 fM range. LOD was calculated to be 1 pM in buffer solution based on statistical analysis. Different concentrations of three target genes, (D) AMACR, (E) PCA3, and (F) PSMA, were spiked into urine from healthy individuals.

Results show very similar to experiments in buffer solution. LODs for AMACR, PCA3, and PSMA were 10 pM, pM, 10 pM.

To determine the influence of non-specific binding, we performed experiments with different amounts of MBs (6,000,000 capture oligos per MB) without any target gene (**Figure 3.14**). At all concentrations of MBs (from 0.033 amol to 66 amol) the normalized intensities in the assay were statistically indistinguishable, indicating that non-specific of AuNPs to the MBs is negligible. To see the effect of amount of MBs on the dynamic range of the assay, the assay was performed with less amount of MB (**Figure 3.15**). There was no significant difference observed in this test either. This data showed a possibility of using less amount of MB in the assay and there should be other factors that plays a role in determining dynamic range of the assay

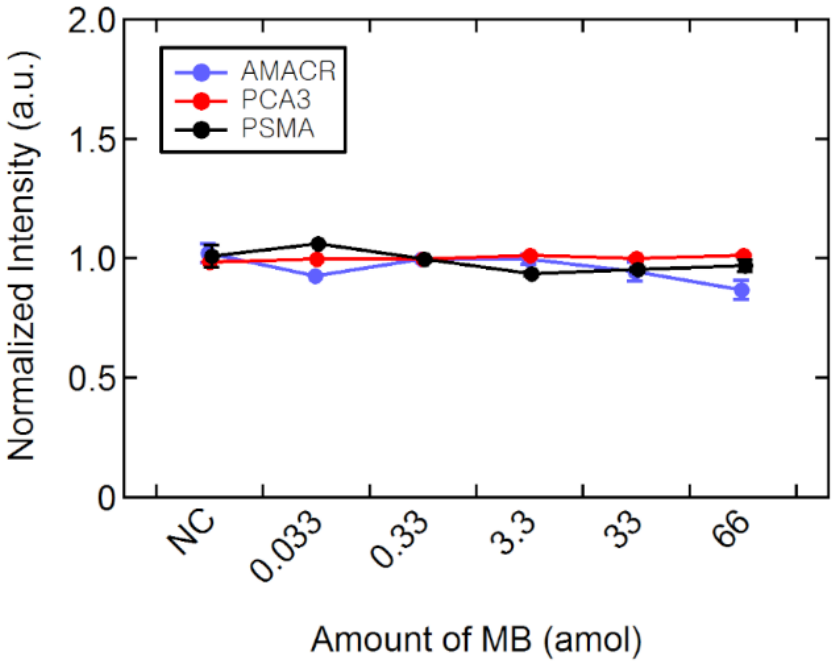

Figure 3.14. To test non-specific binding from NC, different amount of MBs were used

without any target. For all three types of MBs, there was no non-specific binding.

To check the dynamic range of the assay, the upper and lower limits were investigated. The ratio of AuNPs to MPs was around 225, which is optimized to assure enough space between AuNPs for minimizing steric hindrance. Therefore, upper limit of the assay was determined by the amount of AuNPs. Considering a one to one ratio between the target gene and AuNPs, the number of AuNPs used (4.50×10^9) can provides an estimate of the upper (saturation) limit. It was calculated to be about 75 pM. This is a fair estimate since **Figure 3.13A** showed the intensity started to plateau out around 100 pM.

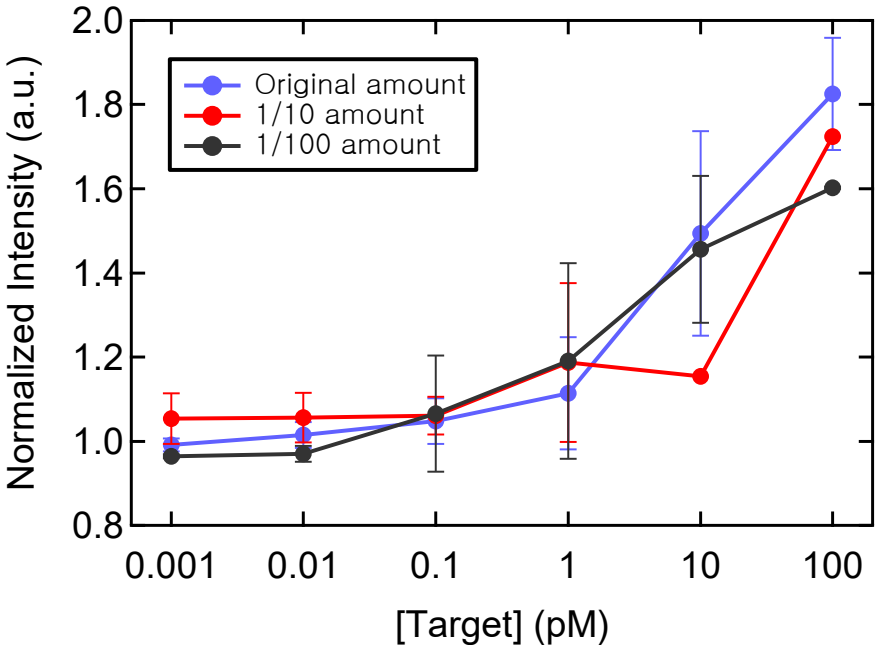

Figure 3.15. Excess amount of MBs are used in the assay. This showed that a less amount of MBs did not affect the dynamic range of the assay (n~3). PCA3 target genes were used in this experiment.

To determine whether the detection limit of the gel reader using the SYBR stain contributes to the lower limit, we used the SYBR detection limit provided by the manufacturer of 60 picograms of double stranded oligos. The lower limit of target concentration is calculated to be around 30 fM by converting SYBR limit in grams into concentration of barcode oligos first, then converting it to concentration of target. This is very reasonable compared to our data shown in **Figure 3.13** where signal started to see elevation around 10-100 fM range.

3.3.7 Single target detection (fusion genes) in buffer solution

To verify whether each AuNP probe binds to target fusion gene specifically, we performed the bio-barcode assay using synthetic target DNA at various concentrations, ranging from 1 nM to 100 aM. Fig. 2a shows the electrophoresis result of the bio-barcode assay for detection of 3 individual target genes in buffer solution. Barcode DNA of different lengths corresponding to respective target gene appeared on native polyacrylamide gel, in agreement with expected molecular weight (target I, 30 bp; target II, 40 bp; target III, 60 bp). Since the final signal was obtained from SYBR Green I fluorophore of dsDNA on gel, accurate quantitative readout can be challenging. The graph for average intensity of each band, however, shows dose-dependent manner (**Figure 3.16**). Moreover, the result showed that bio-barcode assay was able to detect a wide range of concentrations (8-orders of magnitude) with a very low detection limit. At 100 aM target concentration, the intensity of band was higher than the signal for NC. To obtain specific limit of detection value, we measured signal intensity

of each band on a gel using Image J software and calculated actual detection limit for each target gene according to the following equation.[139] (Target I, 1.77; Target II, 1.23; Target III, 1.22)

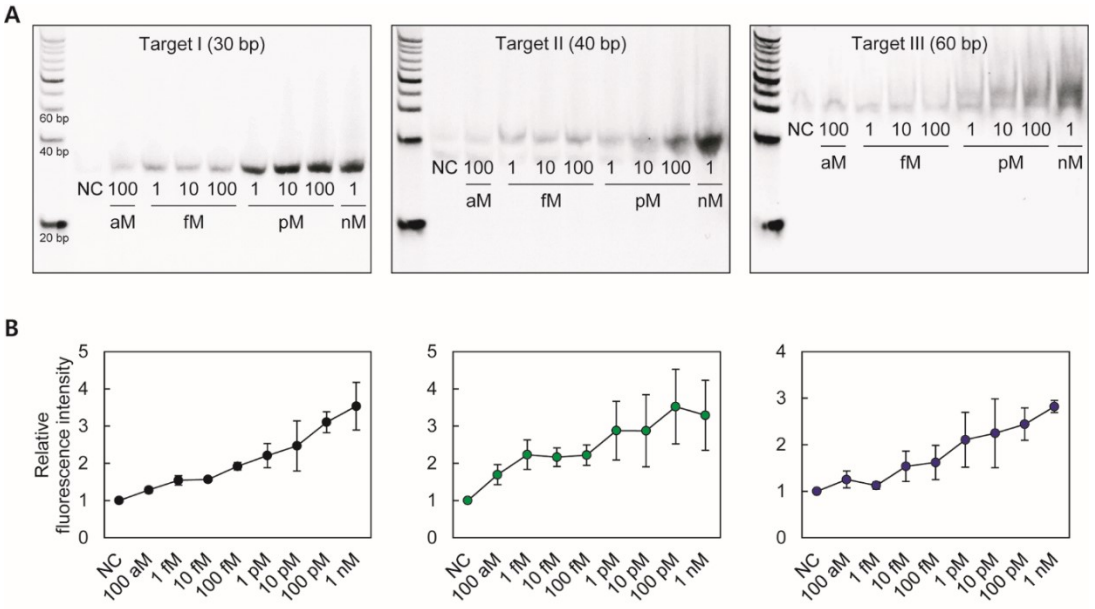

Figure 3.16. Bio-barcode assay for single target detection. (A) The results of single target detection in buffer solution, ranging from 100 aM to 1 nM, are shown. In the gel image, each band shows barcode dsDNA after electrophoresis. (B) Fluorescence intensity of each band is normalized to that of negative control (NC). From left to right, target I, target II, and target III. Error bars indicate standard error of the mean. (n=3)

3.3.8 Multiple target detection (fusion genes) in buffer solution

We tested the capability of the bio-barcode assay to detect multiple target genes with various combinations of target genes (Target I + II, I + III, and II + III) because different length of barcode DNA allows for their separation in a single lane of gel simultaneously. The target mixtures were incubated with three

kinds of magnetic probes and barcode probes for 30 min. The result clearly showed that the bands of barcode dsDNA corresponding to existence of target fusion genes. The detection limit for assay increased in the case of multiplexed assay compared with single target assay. Since the similarity of *TMPRSS2-ERG* fusion genes could make competitive interaction between targets,[140] target capture efficiency of MB and AuNP probes should be decreased. Although competition effect existed, the bio-barcode assay was able to detect three targets at 10 pM (1 fmole) (**Figure 3.17**).

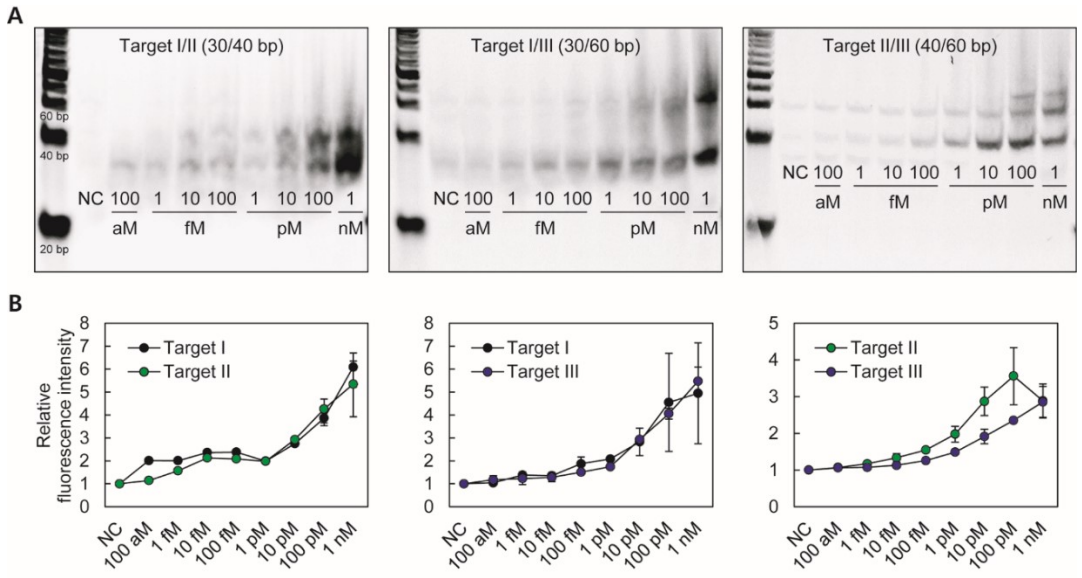

Figure 3.17. Bio-barcode assay for detection of multiple DNA targets. (A) The gel images of multiplexed detection in single assay are shown. Combination of targets (from left to right: target I+II, target I+III and target II+III) are mixed in a buffer solution, ranging from 100 aM to 1 nM of each target. Separation of two different barcode DNA corresponding to different target genes shows capability of multiplexing. (B) Fluorescence intensity of each band is normalized to that of NC. Error bars indicate standard error of the mean. (n=3)

3.3.9 Single target detection (AMACR, PCA3, PSMA) in human urine

Target genes were spiked into healthy human urine to test the feasibility of using the assay with clinical samples. All intensities were normalized to the control (no target) in healthy human urine. Healthy human urine was obtained as a mixture from several healthy individuals with different age, sex, and race. As shown in **Figure 3.13D, E and F**, results suggested that LOD of the assay were slightly lower in the range of 1 pM – 10 pM. This might be due to urine constituents decrease capturing efficiency slightly. The performance of the assay in testing clinical samples showed very similar results compared to experiments in buffer solution. This indicates that urinary components do not affect the performance of the assay significantly. Therefore, using the assay in testing clinical samples seems very promising

3.3.10 Multiple target detection (fusion genes) in human urine

After confirming detection capability of the bio-barcode assay in buffer condition, we tested sensitivity of assay in urine, since urine contains an assortment of inorganic and organic compound including proteins, hormones, and metabolites, the LOD of the assay regarding urine can be decreased due to non-specific binding of urinary components to probes.[141] We found that the bio-barcode assay showed the LOD to be 1 fM (almost the same detection limit to buffer solution), which suggests the bio-barcode assay is able to detect target genes even in urine with high sensitivity (**Figure 3.18**).

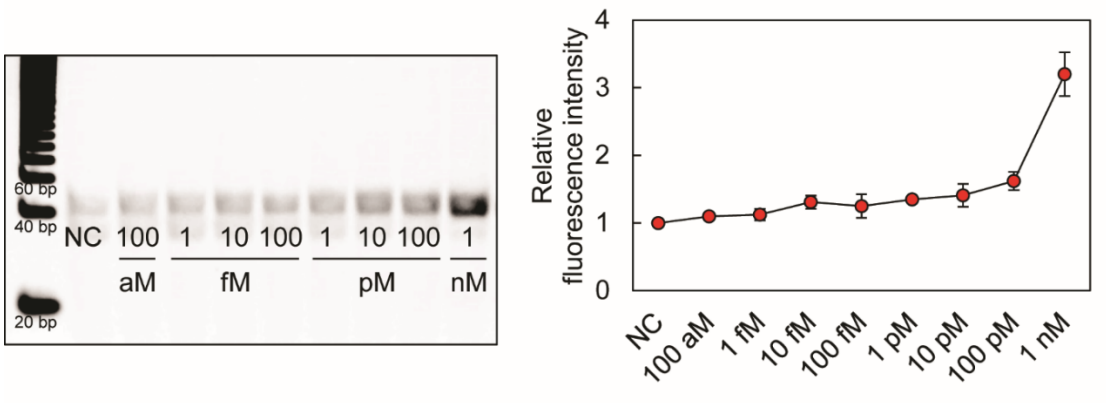

Figure 3.18. The result of bio-barcode assay for synthetic DNA target II in urine. The average fluorescence intensity of the DNA bands at different concentration ranging from 100 aM to 1 nM was shown. Urine of healthy men without any target was used for NC. Error bars indicate standard error of the mean. (n=3)

3.3.11 Determination of fusion gene types in patients' urine

To test whether the bio-barcode assay can be applied in a clinical setting, we detected the fusion genes in various patients' samples (n = 40). This n number is obtained from clinical sample size calculation guides.[142,143] Following equation is used: $n = [(Z\alpha/2 + Z\beta)^2 \times \{(p1\ (1\text{-}p1) + (p2\ (1\text{-}p2))\}12]/(p1 - p2)^2$, where n = sample number, p1 = expression percentage of fusion genes from non-patients (0%), p2 = expression percentage of fusion genes from patients (26% for target I, 86% for target II, 20% for target III), Zα/2 = level of significance, for 5% this is 1.96, Zβ = power, the probability of identifying a real difference with the statistical test and is often taken as 80%, for 80% this is 0.84. At most 31 patients' samples are needed according to this equation. We tested 38 patients' urine samples.

First we compared the bio-barcode assay with well-known RT-PCR for

urinary assay. For the RT-PCR, the purification of RNA from urine is necessary.[144] However, urinary components can affect the purity of RNA, therefore, genetic isolation during the target detection phase in untreated urine is still important.[145] According to previous studies, efficiency of RNA isolation by magnetic particle with complementary sequence to target genes was much higher compared to the conventional Trizol method.[146] Thus, we compared the amount of purified RNA from 10 ml patient urine using the magnetic probe and Trizol solution. Interestingly, even though the magnetic probe captured only specific target RNA, about 500 ng/μL of target RNA was extracted from urine. On the other hand, a 10-times lower amount of total RNA in 10 ml of urine was isolated by the Trizol method. Moreover, the absorbance ratio at 260 nm to 280 nm is much higher in RNA treated with the MB isolation method compared to ratio given by the Trizol method (data not shown). These findings support the fact that magnetic probe capturing system-based bio-barcode assay can enhance the capability for target detection through increased urinary RNA capturing efficiency. Moreover, total assay time for the bio-barcode assay (including gel electrophoresis) was 2 hours, while the RT-PCR required for 4 hours (RNA purification: 90 min, reverse transcription: 50 min, PCR: 80 min, and gel electrophoresis: 30 min).

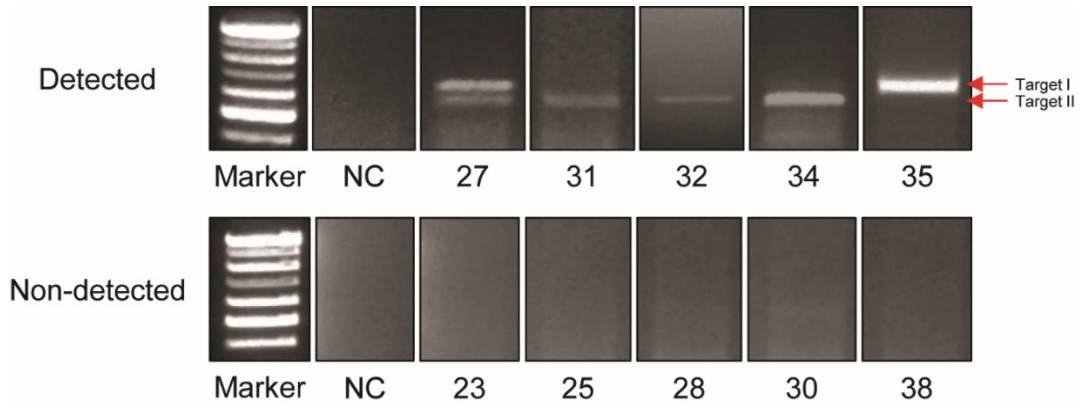

Figure 3.19 Comparison between RT-PCR and bio-barcode assay. "Detected" means patients' sample that were detected fusion genes by the bio-barcode assay. The bands of PCR products, representing target I and II of the *TMPRSS2-ERG*, are well matched with the results of bio-barcode assay in figure S6.

Importantly, two approaches showed the same trend of results; target II was detected by bio-barcode assay and RT-PCR (**Figure 3.19**). To verify whether detected genes was the combination of *TMPRSS2* (exon 1) with *ERG* (exon4), we sequenced the PCR product. The sequencing result agreed well with reported fusion gene sequence,[147] which strongly supported that the bio-barcode assay can specifically determine fusion gene type in urine (**Figure 3.20**).

Furthermore, we observed PSA level in patient urine in order to combine detection of PSA with *TMPRSS2-ERG*. Gleason score of all patients showed almost the same level, which indicates that clinical outcome in patients were similar (**Figure 3.21**). Interestingly, the bio-barcode results showed the diversity of fusion genes while PSA assay showed similar PSA level. (**Figure 3.21 and 3.22**). This result supports the claim that the differential determination of fusion genes in urine of early stage patients can offer more information of patient conditions

and disease progressions. Importantly, although the patient who was treated with the hormone showed an almost zero level of PSA, the fusion gene of target II was detected in the same urine using the bio-barcode assay, which indicates that bio-barcode system can decrease diagnostic error in medicine and can be used to monitoring the prognosis of the disease after patient treatment.

Altogether, the result suggests that the bio-barcode assay can detect three fusion genes in a single assay effectively in a short period of time. Moreover, the assay is cost effective compared to the RT-PCR. This patient friendly technique is a very strong candidate for high throughput screening method for prostate cancer that can give information on genetic diversity.

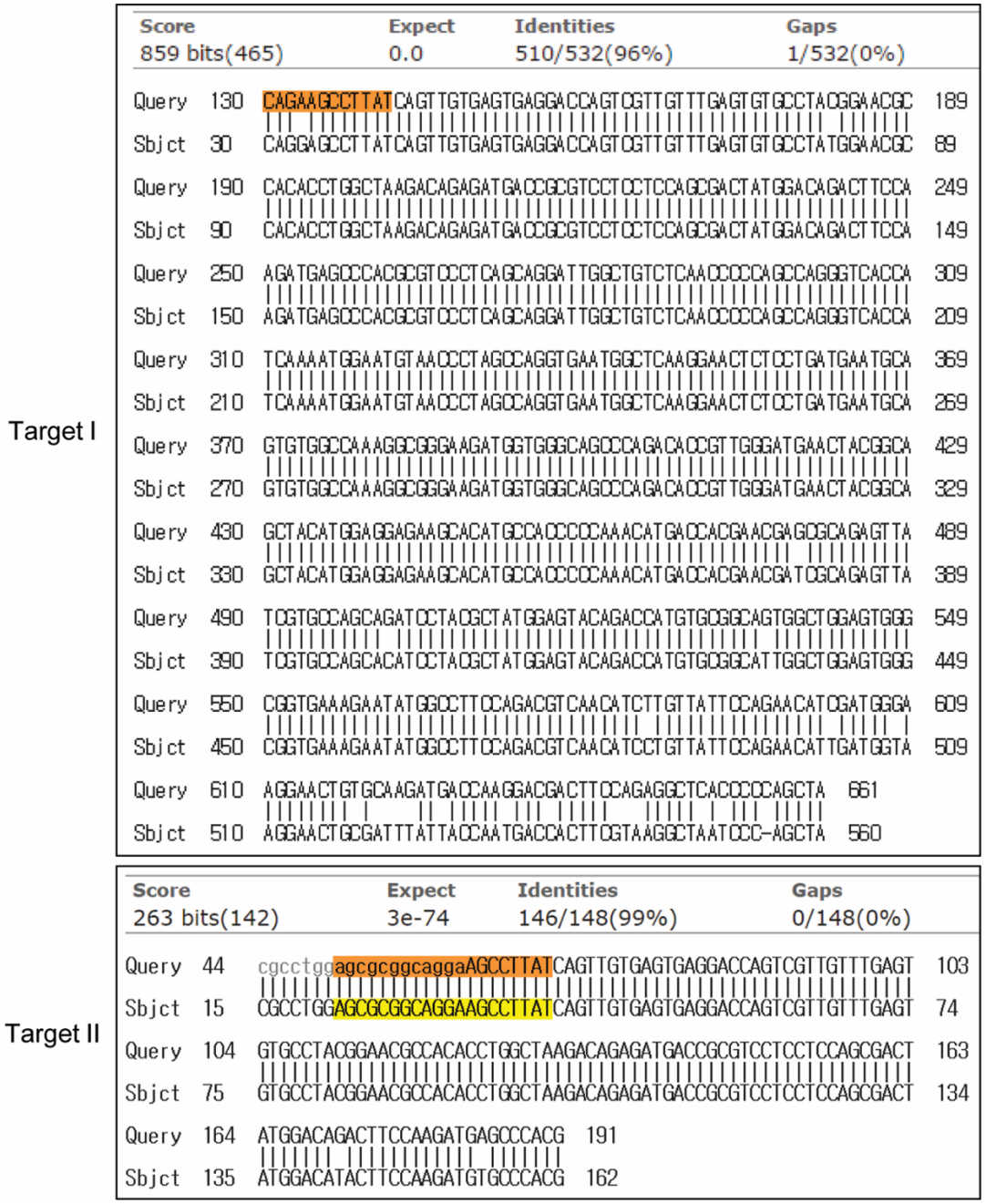

Figure 3.20 BLAST analysis of DNA sequencing result. DNAs after RT-PCR and gel electrophoresis were extracted, purified, and sequenced. BLAST analysis confirmed that the DNA sequence corresponds with *TMPRSS2-ERG* (*TMPRSS2* exon 1/2 + *ERG* exon 4 and *TMPRSS2* exon 1 + *ERG* exon 4). Colored regions indicate target I and II *TMPRSS2-ERG* fusion site.

Clinical Data				*TMPRSS2-ERG*		
Patient	Biopsy Gleason Score	Preoperative PSA (ng/mL)	% Tumor Volume	Target I	Target II	Target III
1	3+3	4.3	-			
2	3+3	4.4	8			
3	3+4	3	-			
4	4+3	5.8	-			
5	3+4	6.8	15			
6	3+4	4.4	5			
7	4+3	7.9	10			
8	Hormone Therapy	0.5	10			
9	4+3	9.3	20			
10	3+4	3.9	7			
11	3+4	7.1	<5			
12	4+3	3.8	20			
13	3+4	11.7	20			
14	3+4	3.8	5			
15	3+4	5.4	10			
16	4+3	10.2	60			
17	4+5	27.9	75			
18	3+3	6.0	5			
19	4+3	9.9	15			
20	4+3	6.4	6			

Clinical Data				*TMPRSS2-ERG*		
Patient	Biopsy Gleason Score	Preoperative PSA (ng/mL)	% Tumor Volume	Target I	Target II	Target III
21	3+4	5.1	10			
22	-	3.0	-			
23	3+4	3.9	25			
24	4+3	5.6	7			
25	3+4	4.3	15			
26	3+4	5.7	10			
27	Hormone Therapy	-	20			
28	3+4	15.9	10			
29	3+4	4.7	10			
30	3+4	4.9	5			
31	4+3	14.6	8			
32	4+3	12.5	30			
33	4+3	3.5	13			
34	3+4	2.0	5			
35	Hormone Therapy	89.4	90			
36	3+4	8.4	18			
37	3+4	3.9	5			
38	Hormone Therapy	-	10			
39	4+4	5.7	15			

Detected Non-detected

Figure 3.21 The results of bio-barcode assay for urine of men with prostate cancer. The urine from healthy human was used as a NC. Biopsy Gleason score is displayed as the sum of Gleason pattern of tumor's primary grade and second grade. PSA level was obtained from patients' blood. Percentage of tumor volume is shown as the ratio of tumor to prostate tissue. The results of *TMPRSS2-ERG* detection is on the right side of each table.

A

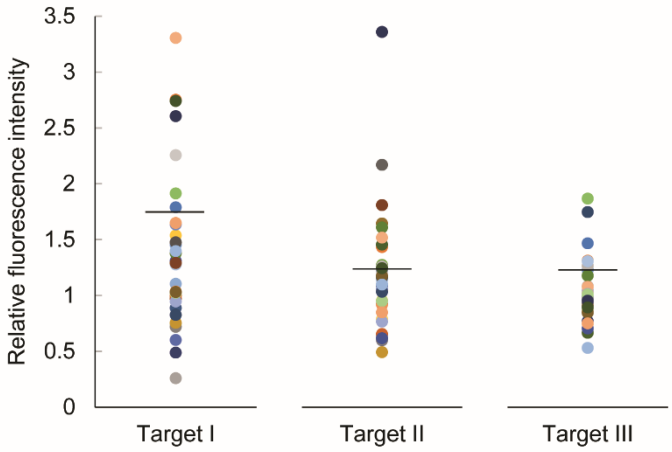

B

Detected	Target I	Target II	Target III
18/39	7 (38.9%)	12 (66.7%)	7 (38.9%)

Figure 3.22 The result of bio-barcode assay for patients' urine with prostate cancer. (A) Relative fluorescence intensity of barcode DNA normalized to NC (urine of healthy men) was shown. Horizontal bars indicate detection limit of each target. (B) Percentage of different types of fusion gene expression was shown. 18 out of 39 patients (46.2%) have at least one type of *TMPRSS2-ERG*. Target II of *TMPRSS2-ERG* was detected in 12 out of 18 patients (66.7%). Both target I and target III fusion genes were expressed in 7 patients (38.9%).

3.4 Conclusions

In this study, oligonucleotide sandwich assay for detecting prostate cancer genomic biomarkers is optimized. Important factors that influence performance of the assay are sequence, length, and number of oligonucleotides. In this study we found that AuNPs conjugated with barcode oligos are more sensitive than MBs conjugated with capture oligos. Obtaining more stable AuNPs with enough amount of barcode oligos for signal amplification is the key for the successful assay. Specific sequences that overlaps at least 20 base pairs with target genes are necessary for the optimal outcome. Also, 5 million capture oligos per MB and 7k barcode oligos per AuNP seemed to perform very effectively without increasing cost too much. Under optimized conditions, clinical samples such as patients' urine can be further investigated in the future to find correlation between expression of genomic biomarkers and clinical outcomes.

Also, we found that the bio-barcode assay improved not only the LOD for fusion gene detection but was also able to specifically target genes in the untreated urine of men with prostate cancer. Importantly, this approach is able to recognize multiple fusion genes in a sample simultaneously because the barcode DNA, with their different lengths, represent the type of fusion gene, and can be visualized at different position on the native polyacylamide gel. Increased sensitivity for fusion genes in the bio-barcode system allows the direct usage of urinary samples for the assay without any cumbersome preparation steps. We anticipate that the assay can be applied in non-invasive diagnosis of prostate cancer through the identification of specific target fusion genes in patient samples as well as in the determination of prostate cancer progression

and aggressiveness.

References

1 Huynh, W. U., Peng, X. G. & Alivisatos, A. P. CdSe nanocrystal rods/poly(3-hexylthiophene) composite photovoltaic devices. *Advanced Materials* **11**, 923-927 (1999).

2 Mattoussi, H. *et al.* Electroluminescence from heterostructures of poly(phenylene vinylene) and inorganic CdSe nanocrystals. *Journal of Applied Physics* **83**, 7965-7974 (1998).

3 Michalet, X. *et al.* Quantum dots for live cells, in vivo imaging, and diagnostics. *Science* **307**, 538-544 (2005).

4 Gao, X. H., Cui, Y. Y., Levenson, R. M., Chung, L. W. K. & Nie, S. M. In vivo cancer targeting and imaging with semiconductor quantum dots. *Nature Biotechnology* **22**, 969-976 (2004).

5 Smith, B. R. *et al.* Real-time intravital imaging of RGD-quantum dot binding to luminal endothelium in mouse tumor neovasculature. *Nano Letters* **8**, 2599-2606 (2008).

6 Information), N. N. C. f. B. *How does the prostate work?*, <https://www.ncbi.nlm.nih.gov/pubmedhealth/PMH0072475/> (2016).

7 Society, A. C. *What is prostate cancer?*, <http://www.cancer.org/cancer/prostatecancer/detailedguide/prostate-cancer-what-is-prostate-cancer> (2016).

8 Torre, L. A. *et al.* Global Cancer Statistics, 2012. *Ca-Cancer J Clin* **65**, 87-108 (2015).

9 Center, M. M. *et al.* International Variation in Prostate Cancer Incidence and Mortality Rates. *Eur Urol* **61**, 1079-1092 (2012).

10 Siegel, R. L., Miller, K. D. & Jemal, A. Cancer Statistics, 2016. *Ca-Cancer J*

Clin **66**, 7-30 (2016).

11 Welch, H. G. & Albertsen, P. C. Prostate Cancer Diagnosis and Treatment After the Introduction of Prostate-Specific Antigen Screening: 1986-2005. *J Natl Cancer I* **101**, 1325-1329 (2009).

12 Kang, B. J. *et al.* Diagnosis of prostate cancer via nanotechnological approach. *Int J Nanomed* **10**, 6555-6569 (2015).

13 Qaseem, A. *et al.* Screening for Prostate Cancer: A Guidance Statement From the Clinical Guidelines Committee of the American College of Physicians. *Ann Intern Med* **158**, 761-+ (2013).

14 Heidenreich, A. *et al.* EAU Guidelines on Prostate Cancer. P5art I: Screening, Diagnosis, and Treatment of Clinically Localised Disease. *Actas Urol Esp* **35**, 501-514 (2011).

15 Catalona, W. J. *et al.* Comparison of Digital Rectal Examination and Serum Prostate-Specific Antigen in the Early Detection of Prostate-Cancer - Results of a Multicenter Clinical-Trial of 6,630 Men. *J Urology* **151**, 1283-1290 (1994).

16 Richie, J. P. *et al.* Prostate-Cancer Screening - Role of Digital Rectal Examination and Prostate-Specific Antigen. *Ann Surg Oncol* **1**, 117-120 (1994).

17 Institute, N. C. *Prostate Cancer Treatment (PDQ®)–Patient Version*, <https://www.cancer.gov/types/prostate/patient/prostate-treatment-pdq> (

18 Partin, A. W. *et al.* Contemporary update of prostate cancer staging nomograms (Partin Tables) for the new millennium. *Urology* **58**, 843-848 (2001).

19 Ilic, D., O'Connor, D., Green, S. & Wilt, T. J. Screening for prostate cancer: an

updated Cochrane systematic review. *Bju Int* **107**, 882-891 (2011).

20 Gambert, S. R. Screening for prostate cancer. *International Urology and Nephrology* **33**, 9 (2001).

21 Stone, N. N. *et al.* Screening for Prostate-Cancer by Digital Rectal Examination and Prostate-Specific Antigen - Results of Prostate-Cancer Awareness Week, 1989-1992. *Urology* **44**, 18-25 (1994).

22 Etzioni, R. *et al.* Overdiagnosis due to prostate-specific antigen screening: Lessons from US prostate cancer incidence trends. *J Natl Cancer I* **94**, 981-990 (2002).

23 Draisma, G. *et al.* Lead times and overdetection due to prostate-specific antigen screening: Estimates from the European randomized study of screening for prostate cancer. *J Natl Cancer I* **95**, 868-878 (2003).

24 H. Ballentine Carter, P. C. A., Michael J. Barry, Ruth Etzioni, Stephen J. Freedland, Kirsten Lynn Greene, Lars Holmberg, Philip Kantoff, Badrinath R. Konety, Mohammad Hassan Murad, David F. Penson, Anthony L. Zietman. EARLY DETECTION OF PROSTATE CANCER: AUA GUIDELINE. 28 (American Urological Association, 2013).

25 Dan Sperling, M., Sperling Medical Group. *Urinary Biomarkers for Prostate Cancer*, <http://sperlingprostatecenter.com/urinary-biomarkers-for-prostate-cancer/> (2016).

26 Nord, M. P., Cluzel, P. & Vionnet, A. Effect of digital rectal examination on prostate specific antigen level. *Presse Med* **25**, 577-580 (1996).

27 Klomp, M. L. F., Hendrikx, A. J. M. & Keyzer, J. J. The Effect of Transrectal Ultrasonography (Trus) Including Digital Rectal Examination (Dre) of the Prostate on the Level of Prostate-Specific Antigen (Psa). *Brit J Urol* **73**, 71-74

(1994).

28 Lechevallier, E., Eghazarian, C., Ortega, J. C., Roux, F. & Coulange, C. Effect of digital rectal examination on serum complexed and free prostate-specific antigen and percentage of free prostate-specific antigen. *Urology* **54**, 857-861 (1999).

29 Crawford, E. D. *et al.* The Effect of Digital Rectal Examination on Prostate-Specific Antigen Levels. *Jama-J Am Med Assoc* **267**, 2227-2228 (1992).

30 Douville, P. & Cembrowski, G. DRE-PSA data revisited: PSA sampling should precede DREs. *Arch Intern Med* **156**, 1352-1352 (1996).

31 Herschman, J. D., Smith, D. S. & Catalona, W. J. Effect of ejaculation on serum total and free prostate-specific antigen concentrations. *Urology* **50**, 239-243 (1997).

32 Nadler, R. B., Humphrey, P. A., Smith, D. S., Catalona, W. J. & Ratliff, T. L. Effect of Inflammation and Benign Prostatic Hyperplasia on Elevated Serum Prostate-Specific Antigen Levels. *J Urology* **154**, 407-413 (1995).

33 Force, M. V. U. S. P. S. T. Screening for prostate cancer: U.S. Preventive Services Task Force recommendation statement. *Annal of Internal Medicine* **157**, 15 (2012).

34 Virginia A. Moyer, U. S. P. S. T. F. Screening for Prostate Cancer: U.S. Preventive Services Task Force

Recommendation Statement. *Ann Intern Med* **157**, 16 (2012).

35 Loeb S., C. W. J. The Prostate Health Index: a new test for the detection of prostate cancer. *Tjerapeutic Advances in Urology* **6**, 4, doi:10.1177/1756287213513488 (2014).

36 Loeb, S. *et al.* The prostate health index selectively identifies clinically

significant prostate cancer. *J Urol* **193**, 1163-1169, doi:10.1016/j.juro.2014.10.121 (2015).

37 Punnen, S., Pavan, N. & Parekh, D. J. Finding the Wolf in Sheep's Clothing: The 4Kscore Is a Novel Blood Test That Can Accurately Identify the Risk of Aggressive Prostate Cancer. *Rev Urol* **17**, 3-13 (2015).

38 Tan, L. G. *et al.* Prospective validation of %p2PSA and the Prostate Health Index, in prostate cancer detection in initial prostate biopsies of Asian men, with total PSA 4-10 ng ml -1. *Asian J Androl*, doi:10.4103/1008-682X.168687 (2016).

39 Tosoian, J. J. *et al.* Use of the Prostate Health Index for detection of prostate cancer: results from a large academic practice. *Prostate Cancer Prostatic Dis*, doi:10.1038/pcan.2016.72 (2017).

40 Hessels, D. *et al.* Predictive Value of PCA3 in Urinary Sediments in Determining Clinico-Pathological Characteristics of Prostate Cancer. *Prostate* **70**, 10-16 (2010).

41 van Gils, M. P. M. Q. *et al.* Detailed analysis of histopathological parameters in radical prostatectomy specimens and PCA3 urine test results. *Prostate* **68**, 1215-1222 (2008).

42 Auprich, M. *et al.* Critical Assessment of Preoperative Urinary Prostate Cancer Antigen 3 on the Accuracy of Prostate Cancer Staging. *Eur Urol* **59**, 96-105 (2011).

43 Ploussard, G. *et al.* Prostate Cancer Antigen 3 Score Accurately Predicts Tumour Volume and Might Help in Selecting Prostate Cancer Patients for Active Surveillance. *Eur Urol* **59**, 422-429 (2011).

44 Salagierski M., S. J. A. PCA3 and TMPRSS2-ERG: Promising Biomarkers in

Prostate Cancer Diagnosis. *Cancers* **2**, 9 (2010).

45 Sroka, W. D. *et al.* Alpha-methylacyl-CoA racemase and hepsin as urinary prostate cancer markers. *Int J Biol Marker* **30**, E401-E406 (2015).

46 Leyten, G. H. J. M. *et al.* Identification of a Candidate Gene Panel for the Early Diagnosis of Prostate Cancer. *Clin Cancer Res* **21**, 3061-3070 (2015).

47 Cornu, J. N. *et al.* Urine TMPRSS2:ERG fusion transcript integrated with PCA3 score, genotyping, and biological features are correlated to the results of prostatic biopsies in men at risk of prostate cancer. *Prostate* **73**, 242-249 (2013).

48 Hessels, D. *et al.* Detection of TMPRSS2-ERG Fusion Transcripts and Prostate Cancer Antigen 3 in Urinary Sediments May Improve Diagnosis of Prostate Cancer. *Clinical Cancer Research* **13**, 5103-5108, doi:10.1158/1078-0432.ccr-07-0700 (2007).

49 Tomlins, S. A. *et al.* Urine TMPRSS2:ERG Fusion Transcript Stratifies Prostate Cancer Risk in Men with Elevated Serum PSA. *Sci Transl Med* **3** (2011).

50 Prior, C. *et al.* Use of a combination of biomarkers in serum and urine to improve detection of prostate cancer. *World J Urol* **28**, 681-686 (2010).

51 Robert, G. *et al.* Rational basis for the combination of PCA3 and TMPRSS2:ERG gene fusion for prostate cancer diagnosis. *Prostate* **73**, 113-120 (2013).

52 Hessels, D. & Schalken, J. A. Urinary biomarkers for prostate cancer: a review. *Asian Journal of Andrology* **15**, 333-339 (2013).

53 Ploussard, G. & de la Taille, A. Urine biomarkers in prostate cancer. *Nat Rev Urol* **7**, 101-109 (2010).

54 Sreekumar, A. *et al.* Humoral immune response to alpha-methylacyl-CoA racemase and prostate cancer. *J Natl Cancer I* **96**, 834-843 (2004).

55 Malusecka E., G. A., Gawkowska-Suwinska M., Behrendt K., Nowicka E., Smolska B., Zajusz A. AMACR Detection in Urine Samples. Lack of Clinical Application in Routine Practice *The Open Prostate Cancer Journal* **3**, 4 (2010).

56 Ouyang, B. *et al.* A Duplex Quantitative Polymerase Chain Reaction Assay Based on Quantification of alpha-Methylacyl-CoA Racemase Transcripts and Prostate Cancer Antigen 3 in Urine Sediments Improved Diagnostic Accuracy for Prostate Cancer. *J Urology* **181**, 2508-2513 (2009).

57 Leonard S Marks, D. G. B. Prostate Cancer Specificity of PCA3 Gene Testing: Examples from Clinical Practice. *Reviews in Urology* **10**, 7 (2008).

58 Merola, R. *et al.* PCA3 in prostate cancer and tumor aggressiveness detection on 407 high-risk patients: a National Cancer Institute experience. *J Exp Clin Canc Res* **34** (2015).

59 Yang, Z., Yu, L. & Wang, Z. PCA3 and TMPRSS2-ERG gene fusions as diagnostic biomarkers for prostate cancer. *Chinese J Cancer Res* **28**, 65-71 (2016).

60 Bussemakers, M. J. G. *et al.* DD3: A new prostate-specific gene, highly overexpressed in prostate cancer. *Cancer Res* **59**, 5975-5979 (1999).

61 Calonge, N. *et al.* Recommendations from the EGAPP Working Group: does genomic profiling to assess type 2 diabetes risk improve health outcomes? *Genet Med* **15**, 612-617 (2013).

62 Rigau, M. *et al.* A Three-Gene Panel on Urine Increases PSA Specificity in the Detection of Prostate Cancer. *Prostate* **71**, 1736-1745 (2011).

63 Tomlins, S. A. *et al.* Recurrent Fusion of TMPRSS2 and ETS Transcription Factor Genes in Prostate Cancer. *Science* **310**, 644-648, doi:10.1126/science.1117679 (2005).

64 Brittany C. Parker, W. Z. Fusion genes in solid tumors: an emerging target for cancer diagnosis and treatment. *Chinese Journal of Cancer* **32**, 594-603 (2013).

65 Mertz, K. D. *et al.* TMPRSS2-ERG fusion prostate cancer is a molecularly distinct estrogen-sensitive subclass of aggressive prostate cancer. *Modern Pathol* **21**, 171A-171A (2008).

66 Wang, J., Cai, Y., Ren, C. & Ittmann, M. Expression of Variant TMPRSS2/ERG Fusion Messenger RNAs Is Associated with Aggressive Prostate Cancer. *Cancer Research* **66**, 8347-8351, doi:10.1158/0008-5472.can-06-1966 (2006).

67 Tomlins, S. A. Urine PCA3 and TMPRSS2: ERG Using Cancer-specific Markers to Detect Cancer. *Eur Urol* **65**, 543-545 (2014).

68 Leyten, G. H. J. M. *et al.* Prospective Multicentre Evaluation of PCA3 and TMPRSS2-ERG Gene Fusions as Diagnostic and Prognostic Urinary Biomarkers for Prostate Cancer. *Eur Urol* **65**, 534-542 (2014).

69 Jang, S. J. Molecular Diagnostics for Detection of Microorganism. *Korean Journal of Clinical Microbiology* **6**, 6 (2003).

70 Stephen A. Bustin, T. N. Pitfalls of Quantitative Real-Time Reverse-Transcription Polymerase Chain Reaction. *Journal of Miomolecular Techniques* **15**, 12 (2004).

71 Ruijter, J. M. *et al.* Amplification efficiency: linking baseline and bias in the analysis of quantitative PCR data. *Nucleic Acids Res* **37** (2009).

72 Huggett, J., Dheda, K., Bustin, S. & Zumla, A. Real-time RT-PCR normalisation; strategies and considerations. *Genes Immun* **6**, 279-284 (2005).

73 Menke, T. B. & Warnecke, J. M. Improved conditions for isolation and quantification of RNA in urine specimens. *Ann Ny Acad Sci* **1022**, 185-189 (2004).

74 Hanke, M., Kausch, I., Dahmen, G., Jocham, D. & Warnecke, J. M. Detailed technical analysis of urine RNA-based tumor diagnostics reveals ETS2/urokinase plasminogen activator to be a novel marker for bladder cancer. *Clin Chem* **53**, 2070-2077 (2007).

75 Tan, S. C. & Yiap, B. C. DNA, RNA, and Protein Extraction: The Past and The Present. *J Biomed Biotechnol* (2009).

76 Zheng, K. W. *et al.* Improved sensitivity and specificity for prostate cancer diagnosis based on the urine PCA3/PSA ratio acquired by sequence-specific RNA capture. *Oncol Rep* **34**, 2439-2444 (2015).

77 Berensmeier, S. Magnetic particles for the separation and purification of nucleic acids. *Appl Microbiol Biot* **73**, 495-504 (2006).

78 Nam, J. M., Thaxton, C. S. & Mirkin, C. A. Nanoparticle-based bio-bar codes for the ultrasensitive detection of proteins. *Science* **301**, 1884-1886 (2003).

79 Thaxton, C. S., Georganopoulou, D. G. & Mirkin, C. A. Gold nanoparticle probes for the detection of nucleic acid targets. *Clin Chim Acta* **363**, 120-126 (2006).

80 Lee, H., Park, J. E. & Nam, J. M. Bio-barcode gel assay for microRNA. *Nat Commun* **5** (2014).

81 Cheong, W. F., Prahl, S. A. & Welch, A. J. A Review of the Optical-Properties of Biological Tissues. *IEEE Journal of Quantum Electronics* **26**, 2166-2185

(1990).

82 Konig, K. Multiphoton microscopy in life sciences. *Journal of Microscopy* **200**, 83-104 (2000).

83 Medintz, I. L., Uyeda, H. T., Goldman, E. R. & Mattoussi, H. Quantum dot bioconjugates for imaging, labelling and sensing. *Nat Mater* **4**, 435-446 (2005).

84 Blackman, B., Battaglia, D. & Peng, X. G. Bright and water-soluble near IR-Emitting CdSe/CdTe/ZnSe Type-II/Type-I nanocrystals, tuning the efficiency and stability by growth. *Chem Mater* **20**, 4847-4853, doi:Doi 10.1021/Cm8000688 (2008).

85 Battaglia, D. & Peng, X. G. Formation of high quality InP and InAs nanocrystals in a noncoordinating solvent. *Nano Letters* **2**, 1027-1030 (2002).

86 Chang, J. Y., Wang, S. R. & Yang, C. H. Synthesis and characterization of CdTe/CdS and CdTe/CdSe core/shell type-II quantum dots in a noncoordinating solvent. *Nanotechnology* **18**, - (2007).

87 Hines, M. A. & Scholes, G. D. Colloidal PbS nanocrystals with size-tunable near-infrared emission: Observation of post-synthesis self-narrowing of the particle size distribution. *Adv Mater* **15**, 1844-1849, doi:Doi 10.1002/Adma.200305395 (2003).

88 Lin, W. *et al.* Highly luminescent lead sulfide nanocrystals in organic solvents and water through ligand exchange with poly(acrylic acid). *Langmuir* **24**, 8215-8219, doi:Doi 10.1021/La800568k (2008).

89 Zimmer, J. P. *et al.* Size series of small indium arsenide-zinc selenide core-shell nanocrystals and their application to in vivo imaging. *Journal of the American Chemical Society* **128**, 2526-2527, doi:Doi 10.1021/Ja0579816

(2006).

90 Xie, R. G. & Peng, X. G. Synthetic scheme for high-quality InAs nanocrystals based on self-focusing and one-pot synthesis of InAs-based core-shell nanocrystals. *Angewandte Chemie-International Edition* **47**, 7677-7680 (2008).

91 Kim, S. *et al.* Near-infrared fluorescent type II quantum dots for sentinel lymph node mapping. *Nature Biotechnology* **22**, 93-97 (2004).

92 Hu, R. *et al.* Functionalized near-infrared quantum dots for in vivo tumor vasculature imaging. *Nanotechnology* **21**, -, doi:Artn 145105

Doi 10.1088/0957-4484/21/14/145105 (2010).

93 Choi, H. S. *et al.* Renal clearance of quantum dots. *Nature Biotechnology* **25**, 1165-1170, doi:Doi 10.1038/Nbt1340 (2007).

94 Galloway, J. F., Park, J., Lee, K. H., Wirtz, D. & Searson, P. C. Exploiting Nucleation and Growth in the Synthesis and Electrical Passivation of CdSe Quantum Dots. *Science of Advanced Materials* **1**, 1-8 (2009).

95 Norako, M. E. & Brutchey, R. L. Synthesis of Metastable Wurtzite CuInSe2 Nanocrystals. *Chem Mater* **22**, 1613-1615, doi:Doi 10.1021/Cm100341r (2010).

96 Guo, Q. *et al.* Development of $CuInSe_2$ nanocrystal and nanoring inks for low-cost solar cells. *Nano Letters* **8**, 2982-2987, doi:Doi 10.1021/Nl802042g (2008).

97 Allen, P. M. & Bawendi, M. G. Ternary I-III-VI quantum dots luminescent in the red to near-infrared. *Journal of the American Chemical Society* **130**, 9240-+ (2008).

98 Cassette, E. *et al.* Synthesis and Characterization of Near-Infrared Cu-In-

Se/ZnS Core/Shell Quantum Dots for In vivo Imaging. *Chem Mater* **22**, 6117-6124, doi:Doi 10.1021/Cm10188lb (2010).

99 Nose, K., Omata, T. & Otsuka-Yao-Matsuo, S. Colloidal Synthesis of Ternary Copper Indium Diselenide Quantum Dots and Their Optical Properties. *J Phys Chem C* **113**, 3455-3460, doi:10.1021/jp809398k (2009).

100 Paszkowicz, W., Lewandowska, R. & Bacewicz, R. Rietveld refinement for CuInSe2 and CuIn3Se5. *J Alloy Compd* **362**, 241-247, doi:10.1016/S0925-8388(03)00592-9 (2004).

101 Zhang, S. B., Wei, S. H., Zunger, A. & Katayama-Yoshida, H. Defect physics of the CuInSe2 chalcopyrite semiconductor. *Phys Rev B* **57**, 9642-9656 (1998).

102 Pesika, N. S., Stebe, K. J. & Searson, P. C. Relationship between absorbance spectra and particle size distributions for quantum-sized nanocrystals. *J Phys Chem B* **107**, 10412-10415 (2003).

103 Pesika, N. S., Stebe, K. J. & Searson, P. C. Determination of the particle size distribution of quantum nanocrystals from absorbance spectra. *Adv Mater* **15**, 1289-1291 (2003).

104 Park, J., Lee, K. H., Galloway, J. F. & Searson, P. C. Synthesis of Cadmium Selenide Quantum Dots from a Non-Coordinating Solvent: Growth Kinetics and Particle Size Distribution. *J Phys Chem C* **112**, 17849-17854 (2008).

105 Dubertret, B. *et al.* In vivo imaging of quantum dots encapsulated in phospholipid micelles. *Science* **298**, 1759-1762 (2002).

106 Cormode, D. P., Jarzyna, P. A., Mulder, W. J. M. & Fayad, Z. A. Modified natural nanoparticles as contrast agents for medical imaging. *Adv Drug Deliver Rev* **62**, 329-338, doi:10.1016/j.addr.2009.11.005 (2010).

107 Moyer, V. A. Screening for Prostate Cancer: U.S. Preventive Services Task Force Recommendation Statement. *Annals of Internal Medicine* **157**, 120-134, doi:10.7326/0003-4819-157-2-201207170-00459 (2012).

108 Wilt, T. J. *et al.* Systematic Review: Comparative Effectiveness and Harms of Treatments for Clinically Localized Prostate Cancer. *Annals of Internal Medicine* **148**, 435-448, doi:10.7326/0003-4819-148-6-200803180-00209 (2008).

109 Grossfeld, G. D. & Carroll, P. R. Prostate Cancer Early Detection: a Clinical Perspective. *Epidemiologic Reviews* **23**, 173-180 (2001).

110 Kang, B. J. *et al.* Diagnosis of prostate cancer via nanotechnological approach. *International Journal of Nanomedicine* **10**, 6555-6569, doi:10.2147/IJN.S91908 (2015).

111 Tosoian, J. J. *et al.* Intermediate and Longer-Term Outcomes From a Prospective Active-Surveillance Program for Favorable-Risk Prostate Cancer. *J Clin Oncol* **33**, 3379-+ (2015).

112 Jeong, S. *et al.* Integrated Magneto–Electrochemical Sensor for Exosome Analysis. *ACS Nano* **10**, 1802-1809, doi:10.1021/acsnano.5b07584 (2016).

113 Qaseem, A., Barry, M. J., Denberg, T. D., Owens, D. K. & Shekelle, P. Screening for Prostate Cancer: A Guidance Statement From the Clinical Guidelines Committee of the American College of Physicians. *Annals of Internal Medicine* **158**, 761-769, doi:10.7326/0003-4819-158-10-201305210-00633 (2013).

114 Gaudreau, P. O., Stagg, J., Soulieres, D. & Saad, F. The Present and Future of Biomarkers in Prostate Cancer: Proteomics, Genomics, and Immunology Advancements. *Biomark Cancer* **8**, 15-33, doi:10.4137/BIC.S31802 (2016).

115 Lee, H. *et al.* High throughput differential identification of TMPRSS2-ERG fusion genes in prostate cancer patient urine. *Biomaterials* **135**, 23-29, doi:10.1016/j.biomaterials.2017.04.049 (2017).

116 Lee, H. *et al.* Optical coding of fusion genes using multicolor quantum dots for prostate cancer diagnosis. *Int J Nanomedicine* **12**, 4397-4407, doi:10.2147/IJN.S138081 (2017).

117 Rubin, M. A. *et al.* alpha-Methylacyl coenzyme A racemase as a tissue biomarker for prostate cancer. *JAMA* **287**, 1662-1670 (2002).

118 Lin, P. Y. *et al.* Detection of Alpha-Methylacyl-CoA Racemase (AMACR), a Biomarker of Prostate Cancer, in Patient Blood Samples Using a Nanoparticle Electrochemical Biosensor. *Biosensors (Basel)* **2**, 377-387, doi:10.3390/bios2040377 (2012).

119 Hessels, D. & Schalken, J. A. Urinary biomarkers for prostate cancer: a review. *Asian J Androl* **15**, 333-339, doi:10.1038/aja.2013.6 (2013).

120 Kumar-Sinha, C., Tomlins, S. A. & Chinnaiyan, A. M. Recurrent Gene Fusions in Prostate Cancer. *Nature reviews. Cancer* **8**, 497-511, doi:10.1038/nrc2402 (2008).

121 Lu, B. *et al.* Detection of TMPRSS2-ERG Fusion Gene Expression in Prostate Cancer Specimens by a Novel Assay Using Branched DNA. *Urology* **74**, 1156-1161, doi:http://dx.doi.org/10.1016/j.urology.2009.01.087 (2009).

122 Mortazavi, A. Better together: multiplexing samples to improve the preparation and reliability of gene expression studies. *Nat Meth* **12**, 304-305, doi:10.1038/nmeth.3333 (2015).

123 Hwang, M. P., Lee, J.-W., Lee, K. E. & Lee, K. H. Think Modular: A Simple Apoferritin-Based Platform for the Multifaceted Detection of Pancreatic

Cancer. *ACS Nano* **7**, 8167-8174, doi:10.1021/nn403465a (2013).

124 Chinen, A. B. *et al.* Nanoparticle Probes for the Detection of Cancer Biomarkers, Cells, and Tissues by Fluorescence. *Chemical Reviews* **115**, 10530-10574, doi:10.1021/acs.chemrev.5b00321 (2015).

125 Kim, C. & Searson, P. C. Magnetic bead-quantum dot assay for detection of a biomarker for traumatic brain injury. *Nanoscale* **7**, 17820-17826, doi:10.1039/C5NR05608J (2015).

126 Lee, H., Park, J.-E. & Nam, J.-M. Bio-barcode gel assay for microRNA. *Nat Commun* **5**, doi:10.1038/ncomms4367 (2014).

127 Goluch, E. D. *et al.* A bio-barcode assay for on-chip attomolar-sensitivity protein detection. *Lab Chip* **6**, 1293-1299, doi:10.1039/b606294f (2006).

128 Hill, H. D. & Mirkin, C. A. The bio-barcode assay for the detection of protein and nucleic acid targets using DTT-induced ligand exchange. *Nat Protoc* **1**, 324-336, doi:10.1038/nprot.2006.51 (2006).

129 Oh, B. K., Nam, J. M., Lee, S. W. & Mirkin, C. A. A fluorophore-based bio-barcode amplification assay for proteins. *Small* **2**, 103-108, doi:10.1002/smll.200500260 (2006).

130 Kreyling, W. G. *et al.* In vivo integrity of polymer-coated gold nanoparticles. *Nat Nano* **10**, 619-623, doi:10.1038/nnano.2015.111

http://www.nature.com/nnano/journal/v10/n7/abs/nnano.2015.111.html#supplementary-information (2015).

131 Lee, H., Dam, D. H. M., Ha, J. W., Yue, J. & Odom, T. W. Enhanced Human Epidermal Growth Factor Receptor 2 Degradation in Breast Cancer Cells by Lysosome-Targeting Gold Nanoconstructs. *ACS Nano*, doi:10.1021/acsnano.5b05138 (2015).

132 Nam, J.-M., Stoeva, S. I. & Mirkin, C. A. Bio-Bar-Code-Based DNA Detection with PCR-like Sensitivity. *Journal of the American Chemical Society* **126**, 5932-5933, doi:10.1021/ja049384+ (2004).

133 Hurst, S. J., Lytton-Jean, A. K. R. & Mirkin, C. A. Maximizing DNA Loading on a Range of Gold Nanoparticle Sizes. *Analytical Chemistry* **78**, 8313-8318, doi:10.1021/ac0613582 (2006).

134 Thaxton, C. S. *et al.* Nanoparticle-based bio-barcode assay redefines "undetectable" PSA and biochemical recurrence after radical prostatectomy. *Proceedings of the National Academy of Sciences* **106**, 18437-18442, doi:10.1073/pnas.0904719106 (2009).

135 Gill, R., Goeken, K. & Subramaniam, V. Fast, single-step, and surfactant-free oligonucleotide modification of gold nanoparticles using DNA with a positively charged tail. *Chem Commun* **49**, 11400-11402 (2013).

136 D. Bautista, A. Y., P. Roberts. in *NORGEN BIOTEK CORP.* (2016).

137 de Kok, J. B. *et al.* DD3(PCA3), a very sensitive and specific marker to detect prostate tumors. *Cancer Res* **62**, 2695-2698 (2002).

138 Forootan, A. *et al.* Methods to determine limit of detection and limit of quantification in quantitative real-time PCR (qPCR). *Biomol Detect Quantif* **12**, 1-6, doi:10.1016/j.bdq.2017.04.001 (2017).

139 Armbruster, D. A. & Pry, T. Limit of blank, limit of detection and limit of quantitation. *Clin Biochem Rev* **29 Suppl 1**, S49-52 (2008).

140 Candotti, D., Temple, J., Owusu-Ofori, S. & Allain, J. P. Multiplex real-time quantitative RT-PCR assay for hepatitis B virus, hepatitis C virus, and human immunodeficiency virus type 1. *J Virol Methods* **118**, 39-47 (2004).

141 Ji, A. J. *et al.* Challenges in urine bioanalytical assays: overcoming

nonspecific binding. *Bioanalysis* **2**, 1573-1586, doi:10.4155/bio.10.114 (2010).

142 Rohrig, B., du Prel, J. B., Wachtlin, D., Kwiecien, R. & Blettner, M. Sample Size Calculation in Clinical Trials Part 13 of a Series on Evaluation of Scientific Publications. *Dtsch Arztebl Int* **107**, 552-556 (2010).

143 Sakpal, T. V. Sample Size Estimation in Clinical Trial. *Perspectives in Clinical Research* **1**, 3 (2010).

144 Holyoake, A. *et al.* Development of a Multiplex RNA Urine Test for the Detection and Stratification of Transitional Cell Carcinoma of the Bladder. *Clinical Cancer Research* **14**, 742-749, doi:10.1158/1078-0432.ccr-07-1672 (2008).

145 Eldh, M., Lötvall, J., Malmhäll, C. & Ekström, K. Importance of RNA isolation methods for analysis of exosomal RNA: Evaluation of different methods. *Molecular Immunology* **50**, 278-286, doi:http://dx.doi.org/10.1016/j.molimm.2012.02.001 (2012).

146 Durand, X., Moutereau, S., Xylinas, E. & de la Taille, A. Progensa™ PCA3 test for prostate cancer. *Expert Review of Molecular Diagnostics* **11**, 137-144, doi:10.1586/erm.10.122 (2011).

147 Wang, J., Cai, Y., Ren, C. & Ittmann, M. Expression of variant TMPRSS2/ERG fusion messenger RNAs is associated with aggressive prostate cancer. *Cancer research* **66**, 8347-8351, doi:10.1158/0008-5472.CAN-06-1966 (2006).

Curriculum Vita

Jea Ho Park was born in 1982 in Seoul, Republic of Korea. He moved to US in 1997 and attended Lake Forest Academy in Illinois. He graduated high school, Fairmont Preparatory Academy in California, in 2002.

Jea Ho did his undergraduate in the department of Materials Science and received his Bachelors of Science degree in 2007. During his undergraduate studies, he received the Senior Design award for the outstanding research performance among all seniors in the department.

He received his Master of Science in Engineering degree in 2009 in the same department and during his graduate studies, he began to publish papers (2 publications) and presented many posters (6 posters) at different conferences. He was affiliated and supported by Institute for NanoBioTechnology (INBT) at JHU.

He joined his Ph.D. program in 2011. Before taking a leave of absence (LOA) and work in industry for 2 years, he worked on cancer research using semiconductor nanoparticles, Quantum Dots (QDs). He published 4 papers on *in vitro* and *in vivo* cancer diagnosis using QDs in 3 years and one of them were selected as a cover page in *Small*. After he came back from LOA in 2016, he started a cooperative research project with Korea Institute of Science and Technology in Korea (KIST). For 3 years at KIST, he published 2 papers and one is currently submitted. This research project was focused on *in vitro* cancer diagnosis, targeting genomic cancer biomarkers using gold nanoparticles and oligonucleotides.